

Analyzing dynamics of random pressure fields over bluff bodies using dynamic mode decomposition

Xihaier Luo^{a,*}, Ahsan Kareem^a

^a*NatHaz Modeling Laboratory, University of Notre Dame, Notre Dame, IN 46556, United States*

Abstract

Dynamic wind loads acting on structures by definition are statistically correlated both in space and time. However, conventional approaches for the analysis of distributed aerodynamic loads, such as the proper orthogonal decomposition (POD), can only present relevant spatial pattern that is encapsulated in a set of coherent structures. In this regard, this paper provides an operator-theoretic approach that describes a nonlinear/chaotic dynamical system in a functional space rather than the conventional phase space via the introduction of the Koopman operator. Subsequently, spectral analysis of the Koopman operator provides a spatial-temporal characterization of the time dependent wind loads. We proposed an augmented dynamic mode decomposition (DMD) method to obtain the spectral decomposition results. Specifically, the proposed DMD algorithm is augmented by means of the delay coordinate embedding, and the identified eigen-tuples (eigenvalues, eigenvectors, and time evolution) can not only capture dominant spatial structures but also isolate each structure with a specific frequency and a corresponding growth/decay rate. To demonstrate the unique feature of this approach, we consider learning the evolution dynamics of the random wind pressure field over a scaled model of a finite height prism representing a tall building using limited wind tunnel data. POD analysis of the experimental data is also carried out. We systematically examine the DMD/POD learning results from aspects of algorithm convergence, data sufficiency, and modal analysis, highlighting their specialties and physical interpretations. The ensuing results from the learning process indicate that the proposed method

*Corresponding author. 156 Fitzpatrick Hall, Notre Dame, IN 46556, USA.

Email addresses: `xluo1@nd.edu` (Xihaier Luo), `kareem@nd.edu` (Ahsan Kareem)

can accurately identify a wide range of dynamical mechanisms, which are closely associated with physical phenomena.

Keywords: Tall building, Wind loads, Koopman operator, Dynamic mode decomposition, Coherent structures, Flow mechanism

1. Introduction

Wind loading is naturally probabilistic and is often characterized as a stochastic process, i.e. random field [1, 2]. It is one of the leading concerns in studying wind-induced effects on structures with low fundamental frequencies, such as tall buildings. Extensive research has been conducted out of a need to understand the governing mechanisms buried in the random pressure field [3, 4, 5, 6]. Known under different names such as Karhunen-Loeve expansion, principal component analysis, etc, the proper orthogonal decomposition (POD) is one of the most widely used methods for analyzing random pressure fields in wind engineering [7]. The algorithm involves a procedure that transforms a multi-dimensional isotropic random field into a set of uncorrelated single-dimensional spatial modes that are organized by a sequence of a continuous-valued random process [8, 9]. Because the identified spatial modes are orthogonal to each other, the POD method optimally evaluates the random pressure field in a L_2 norm sense. Consequently, the first a few modes ranked by the energy distribution are generally sufficient to provide a representation of the dominant coherent structures. Despite the POD method has been applied to a variety of engineering scenarios, it is restricted to the second-order statistics and its dimension-reduced representation is limited to a linear transformation regime. Worse yet, the POD method based mechanism distiller fails to integrate dynamical information into identified modes notwithstanding the fact that the random pressure field is continually evolving in time [10, 11].

On the other hand, dynamical systems analysis (DSA) is an interdisciplinary field concerning the temporal behavior of a time-dependent phenomenon. Approaches for the DSA mainly fall into two categories, i.e. geometrical methods and operator-theoretic methods [12, 13]. Recently, there is a strong tendency to move to the equation-free paradigm, that is, the operator-theoretic methods considering the volume of accessible data has increased tremendously in this big data era. The main difference between conventional geometric modeling and recently advanced operator-theoretic mod-

eling lies at the required input information, where the latter only needs data to proceed, while prior knowledge about the system of interest is expected in the geometric analysis [14, 15, 16]. Two properties of being equation-free by means of the operator-theoretic modeling should be noted. First, the conventional geometric modeling establish a descriptive model using available physical laws while the equation-free learning method infers the dynamical mechanisms directly from the data (See Fig. 1 (a)). Secondly, conventional methods describe the dynamical process in the state space, whereas the operator-theoretic modeling lifts the dynamics into an infinite-dimensional Hilbert function space (See Fig. 1 (b)). The superior efficacy of operator-theoretic supported equation-free modeling strikes a new path for inferring governing mechanisms of dynamical systems directly from data. This is especially useful in practice considering the fact that physical equilibrium models are not always available or sometimes partially known, such as the random pressure field over a tall building.

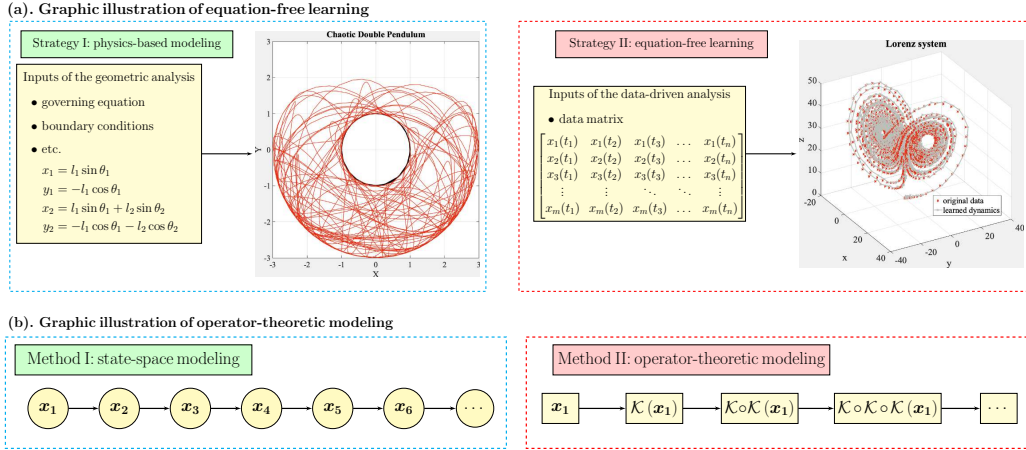


Figure 1: Comparative illustration of the proposed equation-free learning strategy using the operator-theoretic modeling method.

In this work, we present an operator-theoretic approach for distilling hidden dynamical mechanisms directly from experimental data. Specifically, the Koopman operator that is also known as the composition operator is considered [17, 18]. By definition, the Koopman operator explores the evolution of *observables*, which are function actions applied to the state variables. Compared to the conventional state-space modeling, the Koopman operator

lifts the dynamics from state space to the *observable* space. This results in a composition flow map admitted on a function space, and the nonlinear, finite-dimensional dynamics becomes linear but infinite dimensional. Under mild conditions, it has been mathematically proved that the Koopman operator can exactly estimate system dynamics without approximation [14, 15, 16, 18]. For these reasons, we attempt to describe a highly nonlinear dynamical phenomenon, that is, the wind pressure over a tall building through the Koopman operator. Nonlinear wind loads recorded by the synchronously scanned pressure points are thereby transformed into a linear, infinite-dimensional form.

Solving such an infinite-dimensional representation can be formidably challenging, and different methods have been continually developed to obtain a finite-dimensional approximation of the operator. First, generalized Laplace analysis (GLA) introduced by Mezic is an iterative algorithm for solving Koopman modes and eigenfunctions [19]. GLA recursively queries the projected eigenfunctions and subtracts them out from the dynamics. In [20], it was noted that GLA is particularly suitable for applications where a few eigenvalues dominate the entire energy spectrum. Even extensions have been made by considering the inverse expression of the Koopman operator, prior knowledge of the eigenvalues is required to apply the algorithm. More recently, dynamic mode decomposition (DMD), which is an equation-free method and was initially introduced by Schmid out of a need to identify spatial-temporal patterns buried in fluid flows, was found closely connected to the spectral analysis of the Koopman operator [21, 22]. Unlike proper orthogonal decomposition (POD), whose eigenmodes are hierarchically ranked with respect to their energy contribution, DMD performs the eigendecomposition of a linearly dependent operator that is determined by a pair of time-shifted matrices, resulting in a group of periodically oscillating eigenmodes. The resolution scheme is designed in an Arnoldi-algorithm like architecture, where the explicit formulation of connection operator can be saved, greatly improving the computational efficiency. To date, DMD and its advanced variants have been applied to analyze a wide range of dynamical systems [23, 24, 25, 26, 27].

We are interested in characterizing the evolution of random pressure fields utilizing operator-theoretic modeling method, i.e. Koopman operator. The corresponding evolution dynamics will be resolved by means of an augmented dynamic mode decomposition algorithm. The augmentation centers on enriching a limited wind tunnel dataset [28], which is often the

case in experimental research. Specifically, the manifold representing the phase space is embedded into a higher dimensional Euclidean space with topological properties staying unchanged. This topologically equivalent representation is achieved by the introduction of Takens' Embedding Theorem [29]. In particular, delay coordinates containing informative content of the dynamical evolution are effectively exploited. Consequently [30, 31], the augmented dataset is able to provide sufficient information for the data-driven modeling process of dynamic wind loads. We demonstrate the enhanced capability by applying the proposed operator-theoretic modeling strategy to learn random wind pressure fields over faces of a scaled model of a finite height prism representing a tall building. Compare to the classic methods such as POD, learning results indicate our augmented DMD is able to isolate identified dynamical mechanisms with a specific frequency, successfully giving us a glimpse of the dynamical evolution without any prior knowledge of the system.

The remainder of this paper is organized as follows. [Section 2](#) presents the problem of interest and the definition of dynamical mechanisms that need to be distilled. [Section 3](#) offers a detailed discussion on the solution methods, mainly including two parts: Koopman theory and its connection to the dynamic mode decomposition algorithm. A general procedures of numerical implementation computing Koopman eigen-tuple is given. [Section 4](#) covers a comparative study between the conventional and the proposed approach, highlighting the difference from both numerical and physical perspectives. Finally, we conclude in [Section 5](#) with a summary of this work and sheds light on the potential future directions.

2. Problem statement

Consider a measure space $(\mathcal{M}, \mathcal{B}, \mu)$, where $\mathcal{M} \subseteq \mathbb{R}^d$ is the phase space, d is the number of the discretized state variable, \mathcal{B} is a σ -algebra, and μ is a probability measure. Interested in analyzing the random pressure field over tall building structures, we model wind signals as a multivariate random process under the assumption of stationarity and ergodicity [2, 10]. Without loss of generality, let the dynamical wind pressure system take the following form:

$$\frac{d}{dt}(\mathbf{x}) = f(\mathbf{x}(t), \boldsymbol{\theta}) \quad \text{where} \quad t \geq t_1 \quad \text{and} \quad \mathbf{x}(t_1) = \mathbf{x}_1 \quad (1)$$

where $\mathbf{x} = [x_1, x_2, \dots, x_d]^T$ is a column vector denoting the pressure distribution of a building surface $\Omega \in \mathbb{R}^d$, $\boldsymbol{\theta}$ is the parameter vector defining the wind-structure interaction effects, and nonlinear function $f(\cdot)$ is assumed to be sufficiently smooth and linearly bounded, mapping $[t_1, \infty] \times \mathbb{R}^d$ to \mathbb{R}^d (e.g. $f(\cdot)$ satisfies the Lipschitz condition). Then, the dynamical evolution of a discretized wind pressure state $\mathbf{x}(t_k)$, where k is the discrete time index, can be explicitly estimated by integrating Eq. (1):

$$\mathbf{x}(t_k) = \mathbf{T}(\mathbf{x}_{k-1}) = \mathbf{x}(t_{k-1}) + \int_{t_{k-1}}^{t_k} f(\tau, \mathbf{x}(\tau)) d\tau \quad (2)$$

with $t \in [t_{k-1}, t_{k-1} + \tau]$, \mathbf{T} representing the dynamic map, and τ denoting a sufficiently small number. The state variable \mathbf{x} usually locates in a high dimensional space (i.e. $d \gg 1$) due to the desire of acquiring an accurate and detailed profile of wind pressure distributions, where the use of a large number of refined grids or sensors is inevitable (See the data collection step in Fig. 2). Effective treatment of this high-dimensional, nonlinear/chaotic, and dynamical system assumes there exists a low-dimensional manifold \mathcal{S} that embeds Ω into $\mathbb{R}^{d'}$ ($d' < d$) using Borel σ -algebra \mathcal{B} [8, 9].

It should be noted that the discrete formulation of a dynamical system stated in Eq. (2) is more widely used in practice because data collected from either numerical simulation or physical experiments almost always comes in a discrete-time format [1, 13, 12]. Given a sequence consisting of time-ordered snapshots $\mathbf{x}(t_1), \mathbf{x}_2(t_2), \dots$, we are interested in learning a closed and compact embedding of the evolution operator $\mathbf{T} : \mathcal{S} \rightarrow \mathcal{S}$. Hidden dynamical mechanisms that are represented by the a set of *coherent structures* can be correspondingly computed by decomposing the operator held by this low-rank embodiment [14, 15, 16, 19].

Remark (1). In the context of random wind pressure fields, the learned dynamical mechanisms should be able to use identified *coherent structures* to describe the abrupt pressure change. A graphic illustration of the instantaneous evolution associated with the windward face is given in the second row of the red box in Fig. 2. To set up a rigorous problem definition, two important properties should be further clarified. First, *structure* denotes a certain distribution pattern that characterizes the spatial properties inherent in the original topological space \mathbb{R}^d . In the third step of our proposed learning scheme, identified *structures* are encapsulated in a global matrix that contains a complete set of eigenmodes. Secondly, *coherent* implies that this

structure follows a certain developing principle such as recurrence or linear scaling, explaining the pressure evolution from a temporal perspective (See the time evolution plot in Fig. 2).

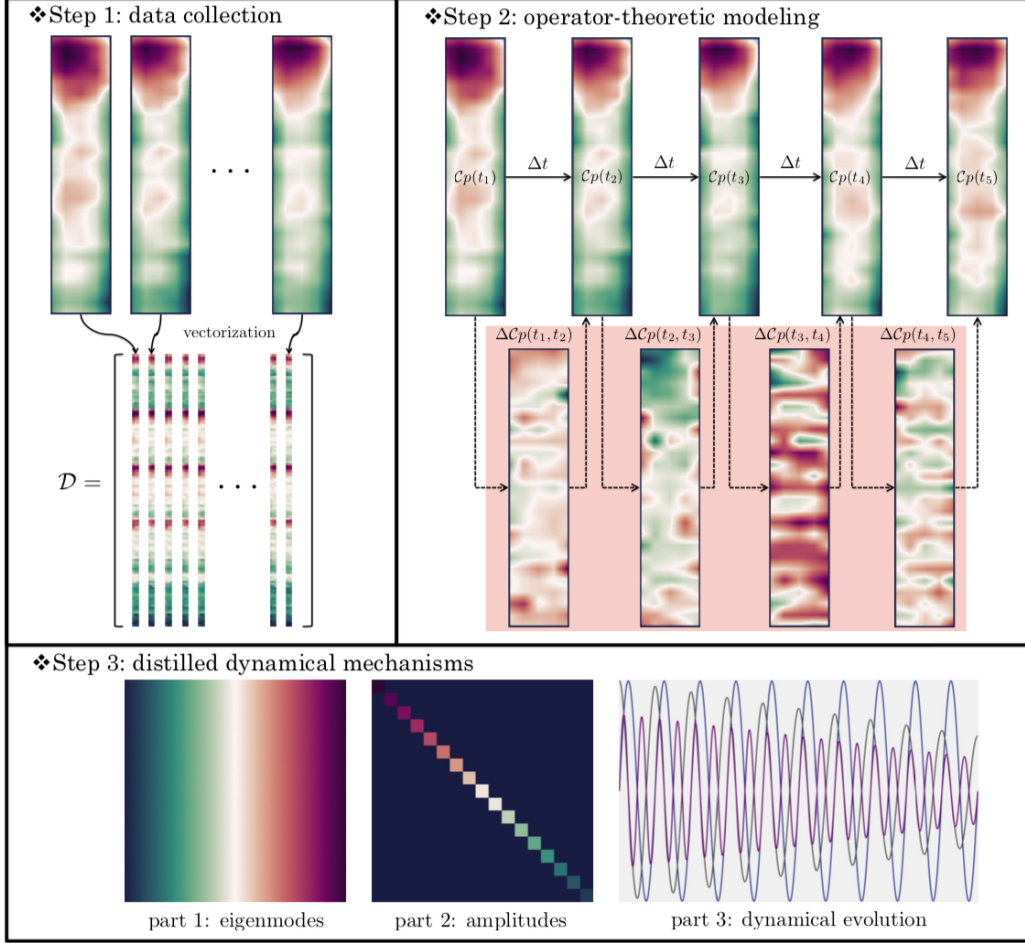


Figure 2: Schematic overview of the proposed equation-free learning with application the random wind pressure field. The overall procedure contains three steps: (1) data collection , (2) operator-theoretic modeling, and (3) dynamics interpretation.

3. Methodology: Koopman operator modeling

This section covers a detailed description of the proposed methodology in terms of handling a dynamical system stated in Eq. (2). Section 3.1 shows how to use Koopman operator to model an evolution process and Section 3.2

presents a numerical scheme for obtaining dynamical mechanisms from the Koopman operator. A complete implementation of the augmented DMD algorithm is given in [Section 3.3](#).

3.1. Spectral analysis of Koopman operator

By definition, Koopman operator \mathcal{K} lifts a dynamical evolution $\mathbf{x}(t_k) = \mathbf{T}(\mathbf{x}_{k-1})$ that is formed in the state space \mathcal{M} to a functional space \mathcal{F} [17, 18, 19, 20]. The empirical observations are accordingly shifted from physical states $\mathbf{x}_1, \mathbf{x}_2, \dots$ to a set of *observables* that are functions of these states. Let function g be a scalar-valued *observable* on the target dynamical system $g : \mathcal{M} \rightarrow \mathbb{C}$, the Koopman operator \mathcal{K} is a linear, infinite-dimensional operator that maps g to a new function $\mathcal{K}g$ given by:

$$\mathcal{K}g = g \circ \mathbf{T}(\mathbf{x}_t) \implies \mathcal{K}g(\mathbf{x}_t) = g(\mathbf{x}_{t+1}) \quad (3)$$

where \circ designates the function composition operator. In analogy with the Heisenberg picture, the linearity of the Koopman operator \mathcal{K} indicates the linear composition operating in a Hilbert function space \mathcal{F} , i.e. $\mathcal{K}(g_1 + g_2) = g_1 \circ \mathbf{T}(\mathbf{x}) + g_2 \circ \mathbf{T}(\mathbf{x}) = \mathcal{K}g_1(\mathbf{x}_t) + \mathcal{K}g_2(\mathbf{x}_t)$, instead of a local linearization that produces tangent planes to the original manifold \mathcal{M} [13, 14, 15, 24]. A nonlinear, finite-dimensional system $\mathcal{M} \rightarrow \mathcal{M}$ is hence fully linearized in the entire basin and well represented in a linear, infinite-dimensional form $\mathcal{F} \rightarrow \mathcal{F}$.

Our primary objective is to analyze and evaluate the dynamical evolution of random wind pressure distributions utilizing spectral properties inherent in the Koopman operator \mathcal{K} , where eigenelements (λ, ϕ) usually appear in pairs and satisfy the eigenvalue equation:

$$\mathcal{K}\phi_j(\mathbf{x}) = \lambda_j\phi_j(\mathbf{x}) \quad \text{where } j = 1, 2, \dots \quad (4)$$

where $\lambda_j \in \mathbb{C}$ is the j^{th} Koopman eigenvalue and $\phi_j(\mathbf{x})$ denotes the paired Koopman eigenfunction, which is a complex-valued *observable* $\phi_j : \mathcal{M} \rightarrow \mathbb{C}$. Let function g be linearly spanned in terms of these Koopman eigenfunctions [21, 22]:

$$g(\mathbf{x}) = \sum_i^{\infty} \phi_i(\mathbf{x}) \vartheta_i \quad (5)$$

with $\vartheta_1, \vartheta_2, \dots$, representing coefficients of expansion. Substitute Eq. (4) and Eq. (5) into Eq. (3), the dynamical evolution can be described by:

$$\mathcal{K}g(\mathbf{x}_t) = \sum_i^{\infty} \lambda_i \phi_i(\mathbf{x}_t) \vartheta_i \quad (6)$$

Obviously, the use of Koopman eigenfunctions supports a linear expansion of the *observable* g . In a similar manner, the eigenfunction expansion of a more general vector-valued *observable* $\mathbf{g} : \mathcal{M} \rightarrow \mathbb{C}^k$ where $\mathbf{g} \doteq [g_1, g_2, \dots, g_k]^T$ takes the expression form of:

$$\mathcal{K}\mathbf{g}(\mathbf{x}_t) = \begin{bmatrix} \sum_i^{\infty} \lambda_i \phi_i(\mathbf{x}_t) \vartheta_{i,1} \\ \sum_i^{\infty} \lambda_i \phi_i(\mathbf{x}_t) \vartheta_{i,2} \\ \vdots \\ \sum_i^{\infty} \lambda_i \phi_i(\mathbf{x}_t) \vartheta_{i,k} \end{bmatrix} = \lambda_i \phi_i(\mathbf{x}_t) \boldsymbol{\vartheta}_i \quad (7)$$

Therefore, when the initial state is determined, the Koopman operator expresses the evolution equation of a dynamical system by means of an infinite summation of sinusoids and exponentials.

Remark (2). λ, ϕ , and ϑ are Koopman eigenelements, each of which discloses a unique physical property of $T : \mathcal{M} \rightarrow \mathcal{M}$. First, expansion coefficients vector $\boldsymbol{\vartheta}_i$ is often referred to as the i^{th} Koopman mode associated with $\phi_i(\mathbf{x})$, containing the spatial information of the dynamical system. $\boldsymbol{\vartheta}_1, \boldsymbol{\vartheta}_2, \dots$, are mathematically the projection of *observables* onto a ϕ_1, ϕ_2, \dots , constitute functional space [24]. Secondly, Koopman eigenvalues $\lambda_1, \lambda_2, \dots$, are indicators of the dynamical evolution. In particular, the real part $\Re(\lambda_i)$ corresponds to the i^{th} magnitude, which determines the growth/decay rate, and the imaginary part $\Im(\lambda_i)$ is the i^{th} phase that controls the frequency of the $\boldsymbol{\vartheta}_i$ [21].

3.2. Computation of Koopman eigen-tuple $(\lambda, \phi, \vartheta)$

Even though Koopman operator provides an explicit modeling strategy of resolving dynamical and oscillatory behavior directly from data, the spectral analysis of \mathcal{K} remains challenging. Currently, dynamic mode decomposition (DMD), which is an equation-free method, serves as the major workhorse solver for obtaining the Koopman eigen-tuple $(\lambda, \phi, \vartheta)$ [13, 21, 23]. DMD approximates the Koopman eigenvalues and eigenmodes by constructing a locally linear operator without inquiring the underlying physics. Let $m \in$

\mathbb{R} be the number of spatial measurements and $n \in \mathbb{R}$ be the number of snapshots, the input matrices of DMD are:

$$\mathbf{Y} = \begin{bmatrix} y_1(t_1) & y_1(t_2) & \dots & y_1(t_{n-1}) \\ y_2(t_1) & y_2(t_2) & \dots & y_2(t_{n-1}) \\ \vdots & \vdots & \ddots & \vdots \\ y_m(t_1) & y_m(t_2) & \dots & y_m(t_{n-1}) \end{bmatrix} \quad \text{and} \quad \mathbf{Y}' = \begin{bmatrix} y_1(t_2) & y_1(t_3) & \dots & y_1(t_n) \\ y_2(t_2) & y_2(t_3) & \dots & y_2(t_n) \\ \vdots & \vdots & \ddots & \vdots \\ y_m(t_2) & y_m(t_3) & \dots & y_m(t_n) \end{bmatrix} \quad (8)$$

Note that t_1, t_2, \dots , are equally distributed during the sampling interval and each element y is defined as $y_j(t_i) \doteq g_j(\mathbf{x}_{t_i})$. A linear dynamical mapping is configured to connect the *observable* matrix \mathbf{Y} and its time-shift pair \mathbf{Y}' :

$$\mathbf{Y}' = \mathcal{A}\mathbf{Y} \quad (9)$$

This linear operator $\mathcal{A} = \mathbf{Y}^\dagger \mathbf{Y}'$ is the key requisite for Koopman eigen-tuple $(\lambda, \phi, \vartheta)$, where \dagger is the Moore-Penrose pseudoinverse. Specifically, when n is sufficiently large and matrices \mathbf{Y}, \mathbf{Y}' are sufficiently informative, the Koopman eigenvalues are identical to the DMD eigenvalues as any eigenfunction of the Koopman operator \mathcal{K} can be linearly spanned in the *observables* space $\phi_i \in \text{span}(g_1, g_2, \dots, g_n)$.

Combine Eq. (8) and Eq. (9), we can rewrite \mathbf{Y} and \mathbf{Y}' in a Krylov subspace form that gives an intuitive formulation illustrating the evolution process:

$$\begin{aligned} \mathbf{Y} &= \{\mathbf{x}, \mathcal{A}\mathbf{x}, \mathcal{A}^2\mathbf{x}, \dots, \mathcal{A}^{n-1}\mathbf{x}\} \\ \mathbf{Y}' &= \{\mathcal{A}\mathbf{x}, \mathcal{A}^2\mathbf{x}, \mathcal{A}^3\mathbf{x}, \dots, \mathcal{A}^n\mathbf{x}\} \end{aligned} \quad (10)$$

To find eigen-tuple $(\lambda, \phi, \vartheta)$ of \mathcal{A} , state variable \mathbf{x}_n is formulated as linear combinations of the columns of \mathbf{Y} . Utilizing the Arnoldi method, the n^{th} snapshot writes as [25]:

$$\mathbf{x}_n = c_1\mathbf{x}_1 + c_2\mathbf{x}_2 + \dots + c_{n-1}\mathbf{x}_{n-1} + \mathbf{r} \quad (11)$$

where $c_i, i = 1, 2, \dots, n-1$ are unknown coefficients and \mathbf{r} is the residual vector. Substitute Eq. (11) into Eq. (9) and together with Eq. (10), we have:

$$\mathcal{A}\mathbf{Y} = \mathbf{Y}\mathbf{C} + \mathbf{r}\mathbf{e}_{n-1}^T \quad (12)$$

where \mathbf{e}_{n-1}^T is the $(n-1)^{th}$ Euclidean unit vector, \mathbf{C} is the companion matrix defined as:

$$\mathbf{C} = \begin{bmatrix} 0 & 0 & \dots & 0 & c_1 \\ 1 & 0 & \dots & 0 & c_2 \\ 0 & 1 & \dots & 0 & c_3 \\ \vdots & \vdots & \ddots & \vdots & \vdots \\ 0 & 0 & \dots & 1 & c_n \end{bmatrix} \quad (13)$$

Numerically, \mathbf{C} approximates the upper Hessenberg representation of \mathcal{A} in a least square sense, guaranteeing the convergence of eigenproblem $\mathbf{C}\phi_{\mathbf{C}} = \lambda_{\mathbf{C}}\phi_{\mathbf{C}}$, that is, eigenvalues of the companion matrix \mathbf{C} is a subset of the Koopman eigenvalues $\lambda_{\mathbf{C}} \subset \lambda_{\mathbf{A}}$ and $\lambda_{\mathbf{C}} \rightarrow \lambda_{\mathbf{A}}$ when the residual vector $\mathbf{r} \rightarrow \mathbf{0}$. Hence, one can first compute the unknown coefficients in \mathbf{C} via the following equation:

$$\mathbf{c} = \mathbf{Y}^\dagger \mathbf{x}_n \quad (14)$$

Next, substitute the resolved \mathbf{c} to Eq. (13) and perform standard eigen-decomposition:

$$\mathbf{C} = \mathbf{V}^{-1} \mathbf{\Lambda} \mathbf{V} \quad (15)$$

where the diagonal elements of $\mathbf{\Lambda}$ are DMD eigenvalues and the corresponding eigenvectors can be determined by:

$$\mathbf{\Phi} = \mathbf{Y}^\dagger \mathbf{V}^{-1} \quad (16)$$

Remark (3). As it is discussed in [25], the use of the companion matrix \mathbf{C} may produce numerically unstable results, especially when the input matrices \mathbf{Y} and \mathbf{Y}' are assembled from contaminated experiment data. For this reason, we provide an alternative implementation scheme where the diagonalization problem presented in Eq. (15) is solved for a well-conditioned matrix that defined by combining the singular value decomposition results and the time-shifted *observable* matrix [13, 23]. Another numerical challenge is directly related to the evolution operator as \mathcal{A} becomes intractable to analyze when it contains too many entries. To solve this problem, a lower rank representation $\tilde{\mathcal{A}}$ is usually constructed by means of the Galerkin projection. A detailed discussion addressing these two challenges as well as their resolution schemes will be provided in the next section.

3.3. Practical implementation and technique issues

The numerical realization of DMD includes matrix decomposition, eigenvalue computation, and data projection. The following gives practical guidance on implementing the DMD algorithm. Specifically, the preliminary work in the context of analyzing wind pressures distribution data starts with assembling *observable* matrices defined in Eq. (8):

$$\begin{aligned}\mathbf{Y} &= [\mathbf{C}_p(t_1), \mathbf{C}_p(t_2), \dots, \mathbf{C}_p(t_n)] \in \mathbb{R}^{m \times n} \\ \mathbf{Y}' &= [\mathbf{C}_p(t_2), \mathbf{C}_p(t_3), \dots, \mathbf{C}_p(t_{n+1})] \in \mathbb{R}^{m \times n}\end{aligned}\quad (17)$$

When this preprocessing task is completed, the DMD algorithm immediately proceeds as follows:

Step 1 : Perform the singular value decomposition:

$$\mathbf{Y} = \mathbf{U}\mathbf{\Sigma}\mathbf{V}^* \quad (18)$$

where $\mathbf{U} \in \mathbb{R}^{n \times n}$, $\mathbf{V} \in \mathbb{R}^{m \times m}$, $\mathbf{\Sigma} \in \mathbb{R}^{n \times m}$, and $*$ denotes the conjugate transpose. This step is very similar to the proper orthogonal decomposition (POD). \mathbf{U} , whose columns are numerical realizations of proper orthogonal modes, follows $\mathbf{U}^*\mathbf{U} = \mathbf{I}$, and \mathbf{V} , whose columns are temporal behaviors, holds $\mathbf{V}^*\mathbf{V} = \mathbf{I}$ (See Appendix A for details).

Step 2 : Determine the r -rank truncation:

$$\mathbf{U}_r = \mathbf{U}[:, 1:r], \mathbf{V}_r = \mathbf{V}[:, 1:r], \mathbf{\Sigma}_r = \mathbf{\Sigma}[1:r, 1:r] \quad (19)$$

The value of parameter r depends on the complexity and dimension of \mathbf{Y} . When \mathbf{Y} are collected from highly nonlinear/chaotic dynamical system, an appropriate choice of r can be decided by means of hard-threshold computing, ensuring sufficient information is kept for investigating system dynamics while noisy perturbation is removed.

Step 3 : Build a r -rank representation $\tilde{\mathcal{A}}$ of the operator \mathcal{A} :

$$\tilde{\mathcal{A}} \doteq \mathbf{U}_r^* \mathbf{Y}' \mathbf{V}_r \mathbf{\Sigma}_r^{-1} \in \mathbb{R}^{r \times r} \quad (20)$$

In this step, the dynamical evolution between \mathbf{Y} and \mathbf{Y}' is seamlessly integrated into $\tilde{\mathcal{A}}$. As mentioned in Remark (3), the philosophy of seeking a low-dimensional structure of \mathcal{A} is to gain computational efficiency. If full-rank based computation is tolerable, one can simply skip step 2 and directly integrate dynamics utilizing SVD results.

Step 4 : Perform the eigendecomposition:

$$[\Phi, \Lambda] = \text{eig}(\tilde{\mathcal{A}}) \quad \text{where} \quad \tilde{\mathcal{A}}\Phi = \Phi\Lambda \quad (21)$$

where columns of Φ are eigenvectors. Λ is a diagonal matrix with non-zero entries representing eigenvalues. The growth/decay rates and corresponding frequencies can be further determined from the eigenvalue sequence $\lambda_1, \lambda_2, \dots$ via $\sigma_i = \frac{\log(\text{Re}(\lambda_i))}{2\pi\Delta t}$ and $\omega_i = \frac{\log(\text{Im}(\lambda_i))}{\Delta t}$ respectively.

Step 5 : Compute DMD modes:

$$\vartheta_k^r = \mathbf{Y}' \mathbf{V}_r \Sigma_r^{-1} \Phi[:, k] \quad (22)$$

It should be addressed that DMD modes computed by Eq. (22) are commonly referred as to the exact DMD modes. An alternative approach is to multiply left singular vectors by eigenvectors $\vartheta' = \mathbf{U}_r \Phi$, where each column of ϑ' is so-called the projected DMD mode. The former definition is closely related to \mathbf{Y} while the emphasis of the second definition is placed on \mathbf{Y}' . By orthogonally projecting ϑ' to the range of \mathbf{Y} , the projected DMD modes can be exactly represented via ϑ .

The overall performance of using DMD algorithm to compute Koopman eigenelements ultimately depends on the initial selection of *observables*. Finding a set of *observables* whose intrinsic dynamics is governed by a linear evolution operator could be fascinating and challenging at the same time. A possible treatment centers on creating a dictionary of *observables* that spans a Krylov subspace of the original phase space. For instance, Hermite polynomials are found to be suitable for problems where state variables x_1, x_2, \dots , are normally distributed. In this paper, we attempt to enrich available *observables* through another perspective. According to the Takens embedding theorem [29, 30, 31], any smooth and compact manifold $\mathcal{M} \in \mathbb{R}^d$, invariant under diffeomorphism T , can be embedded into a $(2d+1)$ dimensional Euclidean space. Therefore, given a scalar sequence of *observable* $y(t_1), y(t_2), \dots$, taken at fixed sampling time. An enriched matrix can be quickly built via delay coordinates:

$$\mathbf{y} = \begin{bmatrix} y(t_1) & y(t_2) & \dots & y(t_j) \\ y(t_2) & y(t_3) & \dots & y(t_{j+1}) \\ \vdots & \vdots & \ddots & \vdots \\ y(t_i) & y(t_{i+1}) & \dots & y(t_{i+j-1}) \end{bmatrix} \quad (23)$$

Likewise, matrices \mathbf{Y} , \mathbf{Y}' from Eq. (8) can be extended to a desirable dimension, and the enriched \mathbf{Y} , \mathbf{Y}' will be used as the input data for the DMD algorithm.

4. Case study

The following case study demonstrates the successful utility of Koopman theory to learn dynamical mechanisms that govern the evolution process of wind pressure distributions over a tall building. A systematic comparison study between the classic POD and proposed DMD method is provided, highlighting the unique ability of Koopman operator in terms of analyzing a highly nonlinear dynamical system.

4.1. Data description

Time-series data containing wind pressure information is obtained from wind tunnel experiments [28], where target tall building of dimension $200m \times 40m \times 40m$ is appropriately scaled to $0.5m \times 0.1m \times 0.1m$. The corresponding rigid model was placed in an open-circuit wind tunnel of dimension $14m \times 1.2m \times 1.0m$ for testing. The mean wind speed profile along the building altitude is defined by a power law exponent of $1/4$, and flow fields were simulated using an hourly average wind speed of $11.1438 m/s$. To collect the data, 500 pressure sensors have been installed on the scaled model. Specifically, there were 125 sensors uniformly distributed on each surface (i.e. a 5×25 distribution manner in terms of the horizontal and vertical axis, respectively), synchronously recording wind effects at a sampling frequency of $1000 Hz$ for a sample period of $32.768 s$. The collected wind pressure data was transformed into a dimensionless expression that is usually referred to as the pressure coefficient C_p , and matrices \mathbf{Y} , \mathbf{Y}' were accordingly built using Eq. (17).

4.2. Convergence study

Given 32768 pressure states, it is highly desirable to provide a reasonable snapshot number N_{snap} for the decomposition analysis, knowing that a small N_{snap} cannot achieve well-converged results while a large N_{snap} would call for an additional amount of computation. A comparative convergence study of POD and DMD methods taking the decomposed spatial and temporal tensor into account is hereby carried out to provide practical guidelines for determining an optimal snapshots number N_{snap}^* for each method.

First, an evaluation metric, which is a function of identified eigenmodes, is used to analyze the convergence behavior of the spatial tensor. Consider two datasets $\mathcal{D}_{\mathbf{p}}^{t_{N_1}} = \{\mathbf{C}_{\mathbf{p}}(t_1), \dots, \mathbf{C}_{\mathbf{p}}(t_{N_1})\}$ and $\mathcal{D}_{\mathbf{p}}^{t_{N_2}} = \{\mathbf{C}_{\mathbf{p}}(t_1), \dots, \mathbf{C}_{\mathbf{p}}(t_{N_2})\}$ that contain pressure signals of the same building surface with a different sampling interval t_{N_1} and t_{N_2} . Two sets of eigenmodes $\Phi^{t_{N_i}} = \{\phi_1^{t_{N_i}}, \phi_2^{t_{N_i}}, \dots\}$, ($i = 1, 2$) can be accordingly computed by means of either POD or DMD method. To measure the relative difference between $\Phi^{t_{N_1}}$ and $\Phi^{t_{N_2}}$, a L_2 norm based metric is defined [26, 27]:

$$\kappa_j = \langle \phi_j^{t_{N_1}} - \phi_j^{t_{N_2}}, \phi_j^{t_{N_1}} - \phi_j^{t_{N_2}} \rangle_{\Omega_{\mathbf{x}}} \quad (24)$$

where $\phi_j^{t_{N_i}}$ indicates the j^{th} eigenmode of $\mathcal{D}_{\mathbf{p}}^{t_{N_i}}$. Usually, t_{N_2} is specified as a constant, serving as the reference point in investigating convergence properties. Then, κ_j simplifies to a general function that exclusively depends on the value of t_{N_1} . By gradually substituting a set of t_{N_1} ordered in an ascend manner into Eq. (24), κ_j traces the convergence behavior regarding the decomposed spatial tensor.

The second evaluation metric is equivalent to the normalized eigenvalue that takes the following form:

$$\lambda_j^\dagger = \frac{\lambda_j}{\sum_{i=1}^n \lambda_i(t_{N_1})} \quad (25)$$

λ_j^\dagger primarily examines the temporal convergence properties of identified coherent structures. It should be further noted that DMD eigenvalues λ_j^{DMD} and eigenmodes ϕ_j^{DMD} are complex-valued. For this reason, complex modulus that measures the magnitude of a tensor from the coordination center to its location in the complex plane is utilized [26, 27]:

$$\begin{aligned} \lambda_j^{DMD} &= \sqrt{(\mathcal{R}e(\lambda_j^{DMD}))^2 + (\mathcal{I}m(\lambda_j^{DMD}))^2} \\ \phi_j^{DMD} &= \sqrt{(\mathcal{R}e(\phi_j^{DMD}))^2 + (\mathcal{I}m(\phi_j^{DMD}))^2} \end{aligned} \quad (26)$$

4.2.1. POD Results

To begin with, $\kappa_i, i = (1, \dots, 4)$ are computed for each building surface, where $t_{N_2} = 30000\Delta t$ and t_{N_1} is a numeric variable that takes value from the sampling interval $[0, t_{N_2}]$. The upper row of Fig. 3 points out the first three fundamental POD modes $\phi_1^{POD}, \phi_2^{POD}, \phi_3^{POD}$ exhibit consistent convergence

properties in all scenarios and the evaluation metric κ decreases dramatically within the time span $[0, 1000\Delta t]$. On the contrary, higher POD modes ϕ_j^{POD} ($j = 4, \dots, 7$) not only converge at a slightly slower pace but also show more random fluctuations during the convergence process. Especially in the two sideward scenarios, κ fluctuates abruptly as $t_{N_1} \rightarrow t_{N_2}$. This reveals the fact that incoherent noises tend to dominate and even likely appear as higher order POD modes. Thus, the POD method can be employed as a denoising technique for preprocessing received signals that are strongly contaminated with noise [8, 9]. The obtained results shown in the second row of Fig. 3 confirm the presence of noise effects, where the first few normalized POD eigenvalues converge at a faster speed with less local perturbation than those held by higher POD modes. Furthermore, the normalized eigenvalues λ_j^\dagger physically represent the mean energy distribution of the wind pressure data. Shown in Fig. 3, some POD modes have similar energy distribution as their correspondingly converged eigenvalues are almost identical. This is algorithmically due to the data projection procedure involved in the POD analysis, and it implies the existence of second-order statistics correlations between projected modes. For instance, mode 2 and mode 3 of the leeward face are a pair of symmetric torsional modes, which are dynamically coupled from an aerodynamics analysis standpoint [3, 4, 7].

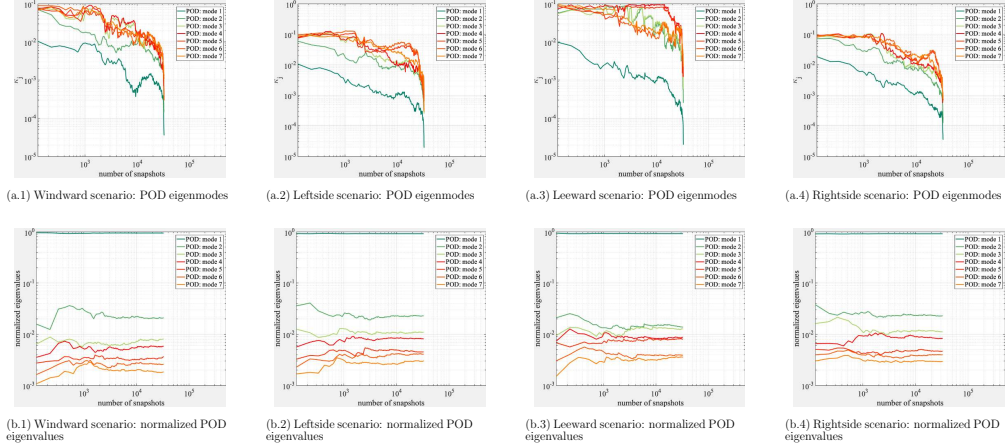


Figure 3: Convergence analysis of POD modes and normalized POD eigenvalues.

4.2.2. DMD Results

In a similar manner, κ_j^{DMD} and normalized DMD eigenvalues λ_j^\dagger are calculated and presented in Fig. 4. According to the results, lower DMD modes exhibit very unstable convergence behavior and higher DMD modes produce random fluctuations rather than decreasing trends. In addition, almost all eigenvalues become wildly oscillated when $N_{snap} > 700$, barely showing any consistent trends. The failure of obtaining converged ϕ_j^{DMD} and λ_j^\dagger is associated with the dynamics integration and eigendecomposition of the DMD algorithm [23, 27]. When the value of snapshots N_{snap} is relatively small, DMD tends to produce a vastly expanded frequency band, where the amplitude spectra covers more isolated frequencies. However, the observed oscillation frequencies of identified DMD modes cluster themselves in a narrowband when N_{snap} increases, thereby obscuring the system identification process as the observed frequencies may often overlap with each other. Such shrinkage property greatly disturbs the pairing between a certain DMD mode and the relative position of its matching λ_j^\dagger with respect to the eigenvalue sequence.

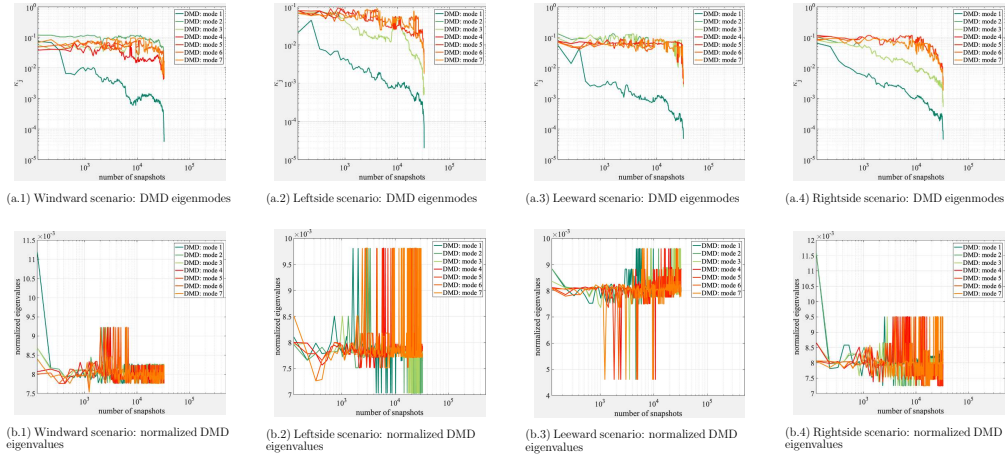


Figure 4: Convergence analysis of DMD modes and normalized DMD eigenvalues.

In Fig. 5, the influence of the snapshot number on the converged spectra is very obvious in all scenarios, where the frequency band shrinks rapidly when $N_{snap} : 300 \rightarrow 500 \rightarrow 700 \rightarrow 900$. In particular, DMD modes are sparsely scattered throughout the interval $[0, 500]$ when $N_{snap} = 300$ while the majority of resolved DMD modes are narrowed within a smaller interval $[0, 100]$ when $N_{snap} = 900$. This reveals the fact that the dominant coherent

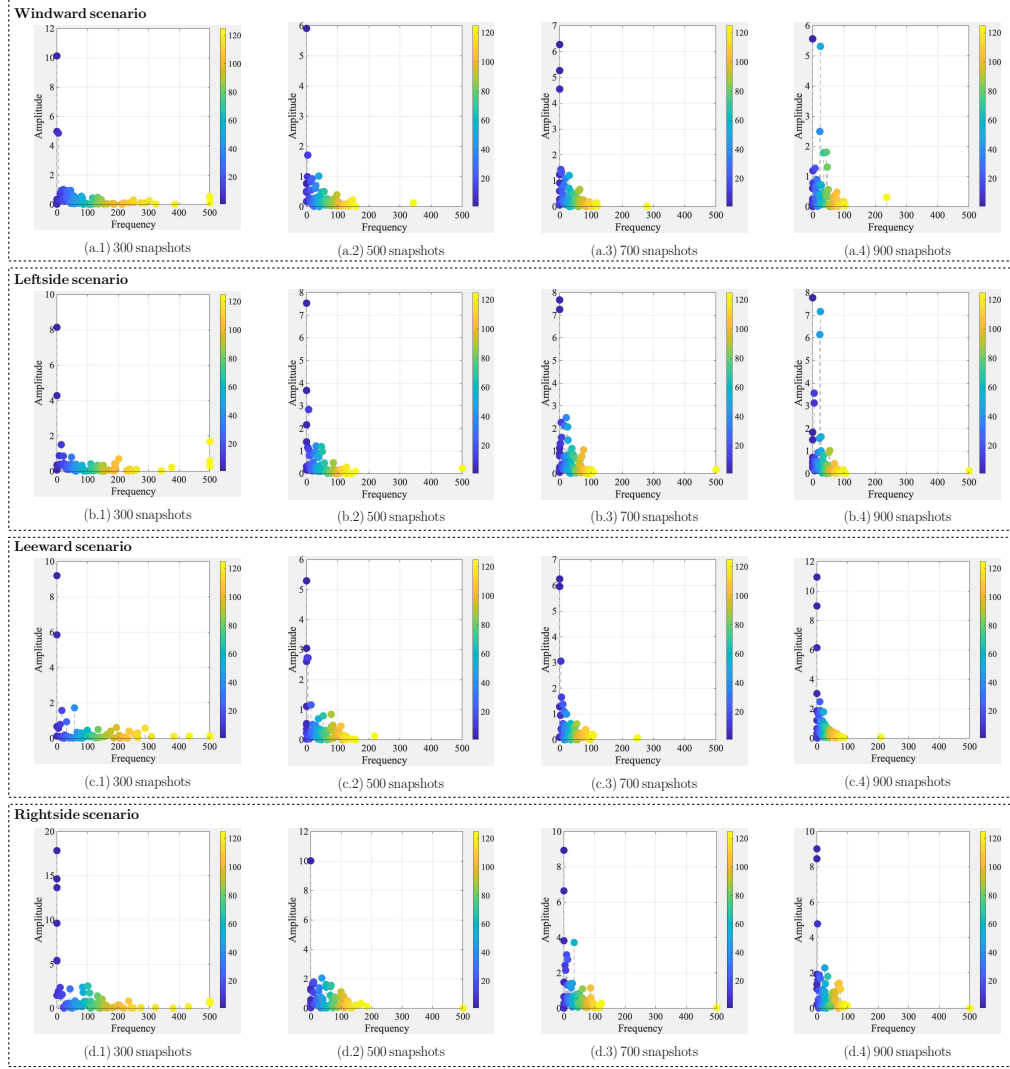


Figure 5: Convergence analysis of DMD energy spectra.

structure explaining random wind pressure evolution is decomposed into a few similar coherent structures whose frequencies may be heavily overlapped [26, 27]. These coherent structures share the dynamical information embedded in the dominant representation identified via a small N_{snap} , but more importantly, they provide different interpretations at a local scale, which are closely related to the small scale turbulence effects. Therefore, converged

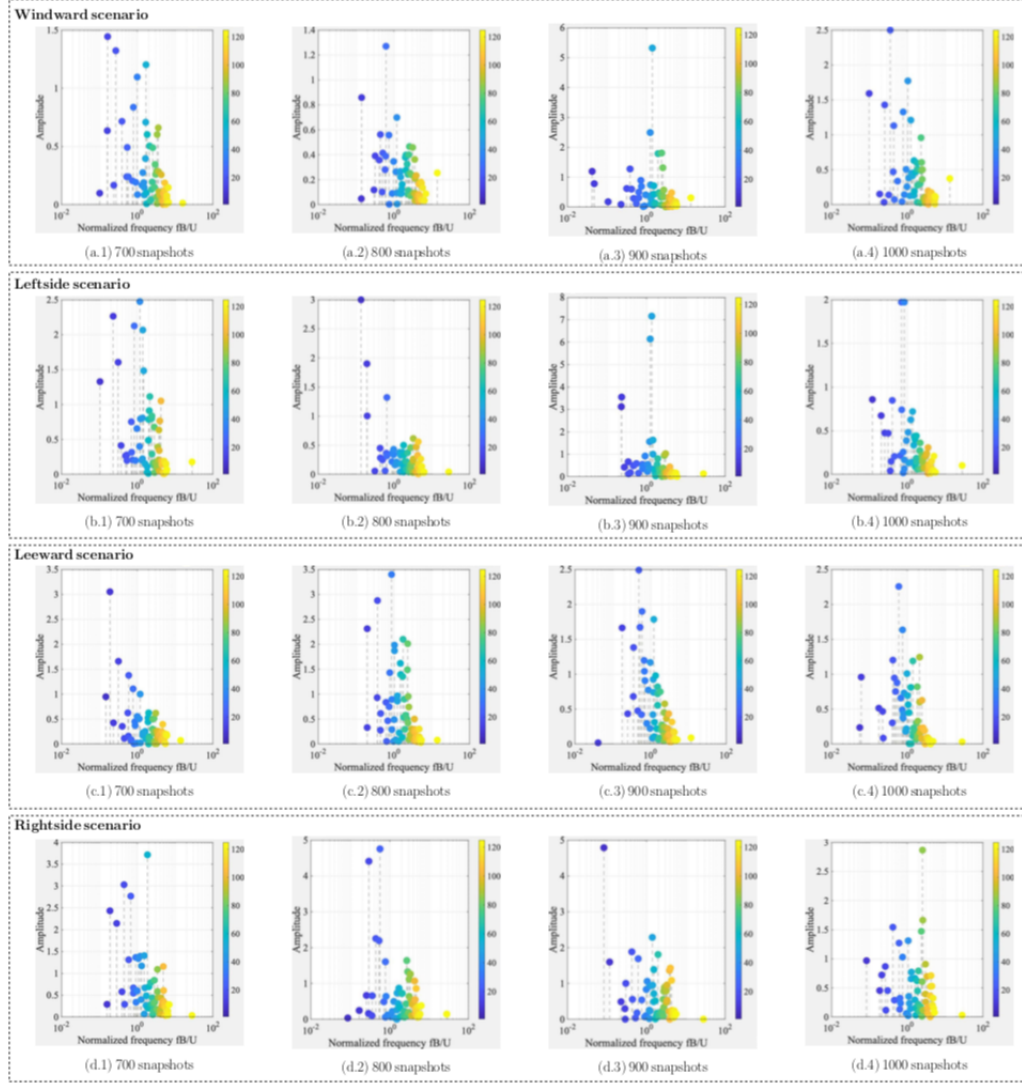


Figure 6: Illustration of different dynamics manifestations inherent in the converged frequency band, where dynamics is a function of N_{snap} .

DMD eigenvalues and eigenmodes are not available in the case of random pressure fields. Instead, we have achieved the convergence of the frequency band and the magnitude of the converged band agrees with the wind loads distribution acting on tall buildings [32, 33].

To understand the random fluctuation happened within this converged

narrowband, Fig. 6 examines the energy spectra computed via $N_{snap} = 700, 800, 900$, and 1000 respectively, where frequencies are normalized by the geometric parameter B and hourly average wind speed U [26, 27]. For example, $N_{snap} = 700$ and $N_{snap} = 900$ yield highly similar energy spectra, indicating the potential existence of converged dynamics from an algorithmic perspective. Two properties of the resolved results should be observed. First, DMD is able to provide physically well-founded spectra results, where the low-frequency region exhibits more complex dynamics and energy variation while the high-frequency region (i.e. yellow dots in Fig. 6) is more unified and stable in against the N_{snap} change. The observation agrees with the natural properties of dynamic wind loads that are often generated from a range of low frequencies while hazards like earthquake tend to contain higher frequency loading components [2, 32, 33]. Moreover, the DMD results are computed using the original wind pressure data without subtracting the mean part, allowing the algorithm to identify the potential coherent structures representing the global force distribution as well as fluctuating wind force generated by wind turbulence. Due to the richness of turbulent dynamics [34, 35], the global coherent structures (i.e. blues dots in Fig. 6) are more scattered, whereas the local DMD modes (i.e. yellow dots in Fig. 6) are relatively more centered. Secondly, DMD modes are not converged even through the frequency band concentrates to a small interval. The simple explanation of this phenomenon is that the complete range and intrinsic types of physical dynamics varies from case to case [26, 27]. One intuitive example would be the long-term wind simulation calls for a different statistical model to describe the probabilistic distribution of the collected time series data when compared to the numerical simulation of downburst winds [36]. Furthermore, wind pressure fields are essentially chaotic due to fluid turbulence. They are described by a multitude of eddies of different sizes and strengths, each of which naturally involves a random process with turbulence coherent structures. Characterization of such turbulence coherent structures requires the development of an accurate spatial-temporal function, confirming the hypothesis that the nature of chaotic dynamics depends on the interval of interest [35, 37], i.e. N_{snap} value. Note that the convergence of the frequency band is by no means an indicator of a well-defined DMD model, rather, it mainly demonstrates the convergence of identified physical properties. To develop a truly reliable model, carrying out a sufficiency study concerning the informative quality of the identified quantities is imperative (See Section 4.3).

4.3. Sufficiency analysis

The main purpose of sufficiency analysis is to find the optimal configuration of low-rank representations that are sufficient to reproduce dynamic wind loads of a prerequisite accuracy level, hence achieving a significant computation reduction compared to the original model. Interested in assessing the amount of information about quantities of interest possessed by the resolved results, we first check the performance of a POD-based reduced order model, then shift the emphasis to the wind pressure data itself as sufficiency by definition is a model-dependent concept, and the sufficiency of input matrices \mathbf{Y} , \mathbf{Y}' are crucial to the success of the DMD algorithm (See [Section 3.3](#) for a detailed discussion).

4.3.1. Sufficiency of the POD method

According to the convergence analysis results ([Fig. 3](#)), the use of a set of 1000 successive snapshots is able to produce well-converged POD modes. Thus, a total of 1000 pressure distribution states $\mathcal{D} = [\mathbf{C}_p(t_1), \dots, \mathbf{C}_p(t_{1000})]$ are analyzed via the conventional proper orthogonal decomposition [[7](#), [8](#), [9](#)]. [Fig. 7](#) shows the ratio of the cumulative sum of the POD eigenvalues, which are normalized by the total energy summation $\sum_{i=1}^{125} \lambda_i$. Despite the fact that the wind pressure is a dynamical system with a combined high nonlinearity and uncertainty, the first eigenvalue ranked by the magnitude captures more than 90 percent of the energy buried in $\mathcal{D} = \mathbf{C}_p(\mathbf{x}, t)$. In practice, the effects of the mean pressure induced wind loads can be accurately obtained from a static analysis utilizing Legendre functions [[38](#)]. The first resolved POD mode representing the mean pressure at different locations is found in good agreement with experimental results [[3](#), [4](#)]. Furthermore, the mean field is extracted and the POD algorithm is performed again using the remaining fluctuation data $\mathcal{D} = \widehat{\mathbf{C}}_p(\mathbf{x}, t)$ to investigate the wind fluctuation effects. In the windward scenario, 7 POD modes are sufficient to reconstruct the pressure fluctuation. Following a similar exponential decay pattern, 20 POD modes are adequate in other three scenarios. The difference reveals the fact that intrinsic complexity of the wind pressure field on the windward face is strongly related to the incoming turbulence, which comes from a wide range of scales [[32](#), [33](#)]. On the contrary, there are more grouped POD modes in the other three scenarios due to dynamics of flow structures under separated shear layers and the wake [[33](#), [39](#)]. Because the higher POD modes mainly account for small pressure fluctuations, a relatively larger number of the POD modes is needed to describe these pressure fields [[6](#), [10](#), [11](#)].

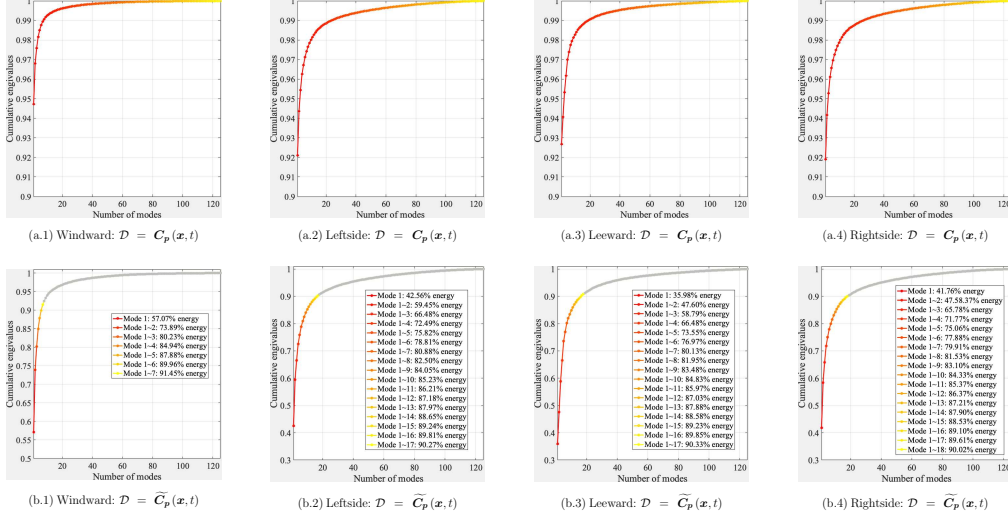


Figure 7: Cumulative eigenvalues versus the number of POD modes. The first row depicts the normalized cumulative energy and the second row outlines the normalized cumulative fluctuation energy.

According to the results given in Fig. 7, the use of a few dominant POD modes $\Phi = \{\phi_1, \phi_2, \dots\}$ is adequate to reproduce an accurate approximation of $\widetilde{\mathbf{C}}_p(\mathbf{x}, t)$ as eigenvectors computed from the covariance matrix minimize the reconstruction error $\mathcal{J}(\mathbf{v})$ (See Appendix A for details). A reduced order model (ROM) is hereby built utilizing a limited number of extracted POD modes. Specifically, the Galerkin projection method is considered, where the wind dynamics of interest is projected onto a subspace spanned via the computed POD modes, that is, $\mathbf{C}_p \in \text{span}\{\phi_1, \dots, \phi_r\}$. Then, the POD-ROM describes the evolution of the wind pressure by mapping the lower dimensional manifold back to the original high dimension $\widetilde{\mathbf{C}}_p(\mathbf{x}, t) \approx \sum_{j=1}^M a_j(t) \phi_j(\mathbf{x})$ [40]. Even though there is no guarantee that a POD-ROM built using the first r eigenmodes will approximate the system well [9, 10, 40], it can be seen from Fig. 8 that a truncated representation utilizing the first 10 POD modes could adequately capture the main pattern of $\widetilde{\mathbf{C}}_p(\mathbf{x}, t)$ over the windward surface. Because the magnitude of eigenvalues decreases rapidly, a POD-ROM via 30 POD modes is well calibrated for the description of the nonlinear correlation in data. A small contribution by high order POD modes, i.e. $\phi_i, i > 70$, is observed thereafter. It should be noted that the projected dynamics are evolving in a linear subspace because of the

balanced truncation, which limits the accuracy of the POD-ROM [40]. To build a more effective ROM for handling nonlinear/chaotic dynamics of slow decaying Kolmogorov widths, one can consider using advanced projection schemes such as least-squares Petrov-Galerkin projection or neural networks, which by definition gives rise to the nonlinear model reduction [41, 42].

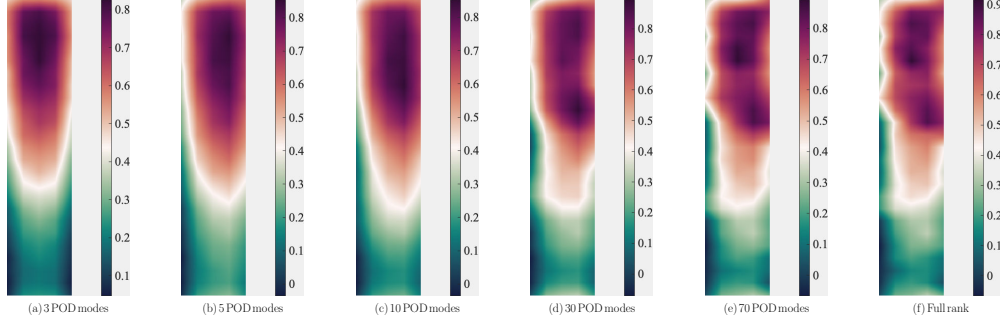


Figure 8: Field reconstruction of an instantaneous snapshot, where $t = 1000\Delta t$. The POD algorithm is performed using 3000 snapshots with a different truncation number. The full rank means there all POD modes are used and the reconstruction results are identical to the original experiment data.

4.3.2. Sufficiency of the DMD method

In a similar manner, elements in the complex-valued sequence $\lambda_1^{DMD}, \dots, \lambda_{125}^{DMD}$ are sorted by the absolute magnitude of the real part in descending order to visualize the cumulative DMD eigenvalues. Specifically, we conducted 4 trials for each building surface (16 in total), exploring the effects of the embedding number on the decomposition results [29, 30, 31]. In Fig. 9, these 16 trials share several underlying trends that can be broadly summarized in three-fold. First, the red line representing the complex modulus summation pattern gradually converges to diagonal reference line as the Takens embedding number increases. The reference line is a simple linear function with zero intercepts and the slope is determined by the truncation number n , i.e. $y = 1/125x$. In comparison with the POD results, rapid growth of the cumulative eigenvalues is undetected in ordered DMD results $\mathcal{R}e(\lambda_1^{DMD}) > \mathcal{R}e(\lambda_2^{DMD}) > \dots$ (See the blue lines in Fig. 9). The reasoning is associated with the essence of the Koopman operator, which transforms a nonlinear, finite-dimensional system to a linear, infinite-dimensional structure [17, 18, 20]. The original nonlinear/chaotic dynamics is projected onto an infinite number subspace $\mathcal{S}_1, \mathcal{S}_2, \dots$, where each subspace \mathcal{S} contains a

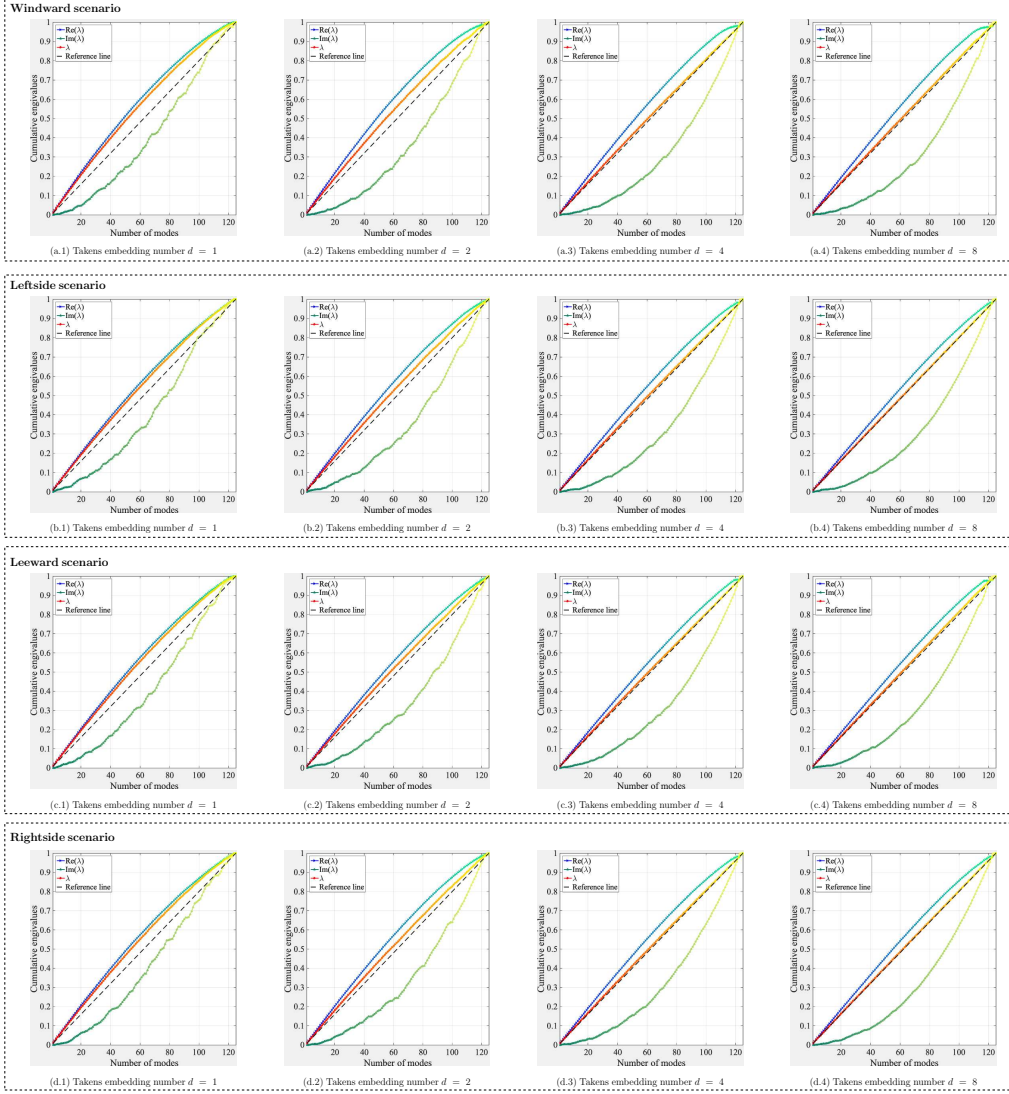


Figure 9: Cumulative eigenvalues versus the number of DMD modes. The straight reference line is a linear function whose independent variable is the number of DMD modes, the dependent variable is the normalized cumulative eigenvalues, and the intercept is 0.

certain type of physical phenomenon that is further spanned by an infinite Koopman modes, whose eigenvalues are highly similar [23, 24, 25]. Moreover, when Takens embedding number $n > 1$, the spatial dimension increases from 125 to $125 \times n$. A small part of the cumulative summation is prone to be

linear from a numerical computation perspective [15, 18]. As we will discuss the modal analysis of DMD modes in the following [Section 4.4.2](#), a DMD mode computed from the original data set ($d = 1$) manages a set of DMD modes computed using the embedded data ($d > 1$). The physical interpretation is the embedding process reinforces the dynamics buried in the dataset by enriching the details, cascading a DMD mode to a set of DMD modes sharing a general spatial pattern but holding different distribution emphasis. Hence, a linearly increasing pattern is observed. Secondly, both real and imaginary lines appear to be smoother when n becomes large, affirming the enrichment effects brought by the delay coordinates. Thirdly, the green line graphically denoting the imaginary information of DMD eigenvalues is a downward convex function. Because the imaginary part corresponds to the phase information [13, 21, 22], that is, the frequency content, the gradients of this function indicate that identified coherent structures whose properties are dramatically evolving in time tend to have larger amplitudes. This is in line with the turbulence modeling theory where large eddies are rapidly developing while small eddies grow with a relatively bigger frequency [34, 43].

[Fig. 10](#) shows the distribution of DMD eigenvalues $\lambda_1, \dots, \lambda_{125}$. In practice, the DMD eigenvalues represent evolution dynamics between subsequent snapshots [23, 25]. Eigenvalues are found to be unstable if its complex modulus is greater than 1 (i.e., are located outside the unit circle) and eigenvalues are deemed as stable or neutrally stable if $\sqrt{\mathcal{R}e(\lambda_i)^2 + \mathcal{I}m(\lambda_i)^2} \leq 1$ (i.e., are located inside or on the unit circle). Without Takens embedding ($d = 1$), both stable and neutrally stable DMD modes have been identified. Though the majority of DMD modes are expected to be located at the circular perimeter, most DMD eigenvalues are away from the stable region, implying the wind tunnel data is strongly contaminated with noisy [13, 23]. To diminish the noise induced data distortion, we augment the dataset by the introduction of the delay coordinates. The resulting distributions are compared in [Fig. 10](#). It can be easily seen that the augmented DMD effectively mitigates the noise influence as $\lambda_1, \dots, \lambda_{125}$ are gradually pushed to the circle boundary. Even with a slightly enhanced topological space $n = 8$, subspace projection results are significantly improved in all scenarios. This Takens' embedding based augmentation agrees with the theory of the dynamic mode decomposition as only neutrally stable eigenvalues should be identified if sufficiently long observations are fed to the DMD algorithm [30, 31].

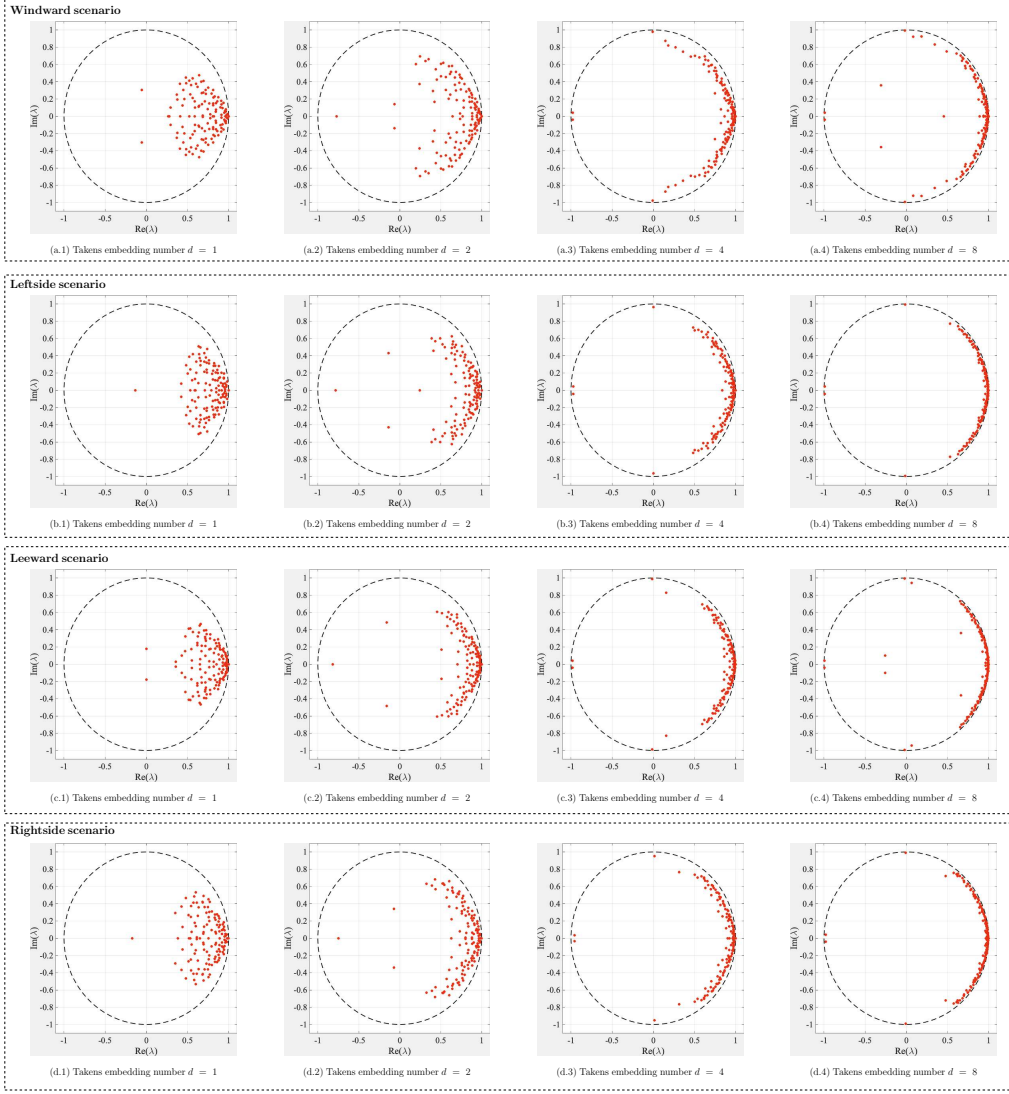


Figure 10: Scatterplot of the DMD eigenvalues $\lambda_1, \dots, \lambda_{125}$.

The physical insights obtained from this sufficiency analysis can be summarized as: (1) it may not be straightforward to pick physically relevant modes with respect to the dynamical significance of each mode since truncated eigenvalues are almost linearly ordered [13, 23]; (2) experiment data with noise needs to be either preprocessed or enhanced, so that system dynamics can be more dominant during system identification. For (1), a ma-

chine learning based method is introduced to determine a group of coherent structures governing the typical dynamical mechanisms (See [Section 4.4.2](#)). For (2), we offer a solution by the adoption of Takens embedding.

4.4. Modal analysis

The goal of modal analysis in the context of analyzing dynamic wind pressure fields is to determine the relationship between the wind loading and the identified eigenmodes. The conventional POD method can provide physical insights connecting POD modes and alongwind, acrosswind and torsional effects, which reasons the wind loads from a spatial distribution perspective. On the contrary, the proposed DMD method explains the nonlinear dynamical phenomenon from a spatial and temporal perspective.

4.4.1. POD modes

Parameterization of POD For the wind pressure example considered here, the POD method is performed independently on each surface, where 1000 snapshots are used during the eigendecomposition process for each trial. Specifically, the singular value decomposition (SVD) is adopted to find an orthogonal set of eigenfunctions [9]. Because the POD algorithm by definition relies on the second-order statistical information, the extracted POD modes provide dominate coherent structures governing the random wind pressure fields from a maximum variance perspective [8, 9]. In particular, $\phi_1^{POD}, \dots, \phi_n^{POD}$ are computed by maximizing the variance of the projected data $tr(\Phi^T \mathbf{C}_p \mathbf{C}_p^T \Phi)$ under the constraint of $\Phi^T \Phi = \mathbf{I}$. To illustrate the resemblance between POD modes and statistical properties of the random pressure fields, a systematic summary of statistical moments is presented in [Fig. 11-Fig. 14](#) in addition to the resolved POD modes as well as the temporal features.

Connections with statistical moments In theory, the mean $\mathbb{E}[|x^1|]$ and the variance $\mathbb{E}[|x^2|]$ describe the location and variability of $\mathbf{C}_p(t)$, respectively. And the skewness $\mathbb{E}[|x^3|]$ and the kurtosis $\mathbb{E}[|x^4|]$ measure the symmetry and flatness of the pressure distribution, accordingly. In all scenarios stated in [Fig. 11-Fig. 14](#), the spatial distribution represented via the first POD mode is very similar to the first-order statistical moment, and the second-order statistical moment may be generally accessed via the combination of a few dominant POD modes. Variability properties included in the skewness and kurtosis, however, cannot be explained, especially in [Fig. 12](#) and [Fig. 14](#), in past due to the focus on second order statistics [3, 10]. In

practice, fluctuations of the wind speed are the major concern for structural engineers in studying the behavior of wind-excited tall buildings [5, 32, 33]. And wind fluctuations are usually quantified by means of the variance or the covariance matrix. In this regard, the POD method is capable of offering reliable results representing the wind effects [4, 7, 33].

Spatial interpretation of POD modes First, the orthogonality of identified modes remains to be a moot point. Noted in [7, 10, 11], such orthogonality is not justifiable from a physical point of view. From a pure identification standpoint, POD may extract coherent structures that are algorithmically deemed as isolated physical patterns embedded in the random pressure field. In particular, POD modes are assumed to be commonly related to the energy distribution of the target phenomena in applications addressing the physical similarity [22, 40]. For instance, ϕ_1, ϕ_2 , and ϕ_3 in Fig. 11 represent the pressure distributions that result in the along-wind overturning moment, whereas similar trends can be observed in Fig. 12-Fig. 14 for ϕ_2 . Moreover, ϕ_2, ϕ_3 in the other three scenarios exhibit distribution patterns related to torsional loads. For example, ϕ_3 in Fig. 13 it shows the negative and positive values are located at the left and right side of the surface respectively, causing a out-of-plane torsion. High order POD modes are more associated with smaller scale features since they are arranged in a decreasing order of eigenvalues. For instance, peak values of ϕ_4 are found around the building edges in all scenarios. Especially in the leeward and two sidewards, min-max values are around corners, suggesting the locates where large pressure oscillations take place. In spite of these physical interpretations, some researchers argue that POD modes are unable to provide subjective physics in terms of explaining a dynamical system [10, 11]. To deploy POD results for optimal control and design, methods such as balanced proper orthogonal decomposition (BPOD) have been developed to establish an input-output relationship for feedback control [40, 41], artificially managing the physics in the POD results.

Temporal interpretation of POD modes The temporal evolution associated with each POD mode is more like stochastic in natural rather than a well-ordered process [20]. The dynamical evolution plots given in Fig. 11-Fig. 14 graphically illustrate the randomness inherent in the temporal pattern. Temporal tensors $a_2(t)$, $a_3(t)$, and $a_4(t)$ are changing abruptly in time, precluding identification of qualitative description of aerodynamic characteristics. This is due to the POD algorithm, where the zero-time-lag covariance matrix is first constructed and then eigendecomposition analysis

is performed using this matrix. Because the wind pressure data is highly nonlinear and the covariance matrix does not contain any evolution information, the resolved POD modes evolve in an abrupt way such that the L_2 norm error involved in the POD formulation is minimized, making it almost impossible to predict the next state in time. Various methods have been developed especially in the field of fluid mechanics to make a nonlinear/chaotic dynamical process controllable and most of these techniques rely on the state-space operator [13, 23]. Next, we will present the modal analysis results by the Koopman operator, which lifts the target dynamics from the state-space to a functional space.

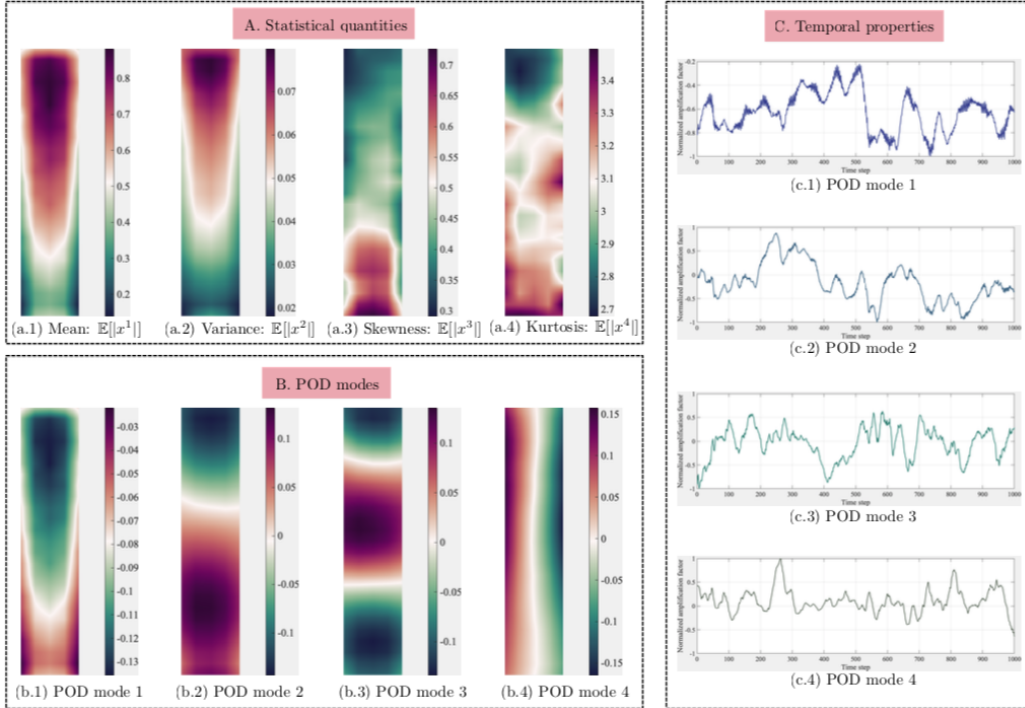


Figure 11: Windward scenario: the decomposed spatial and temporal tensor by the POD algorithm.

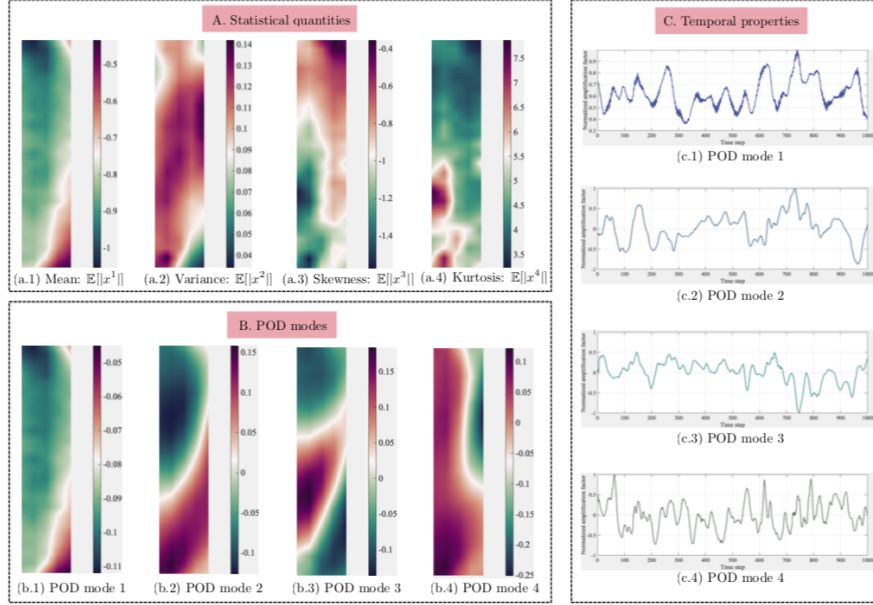


Figure 12: Leftside scenario: the decomposed spatial and temporal tensor by the POD algorithm.

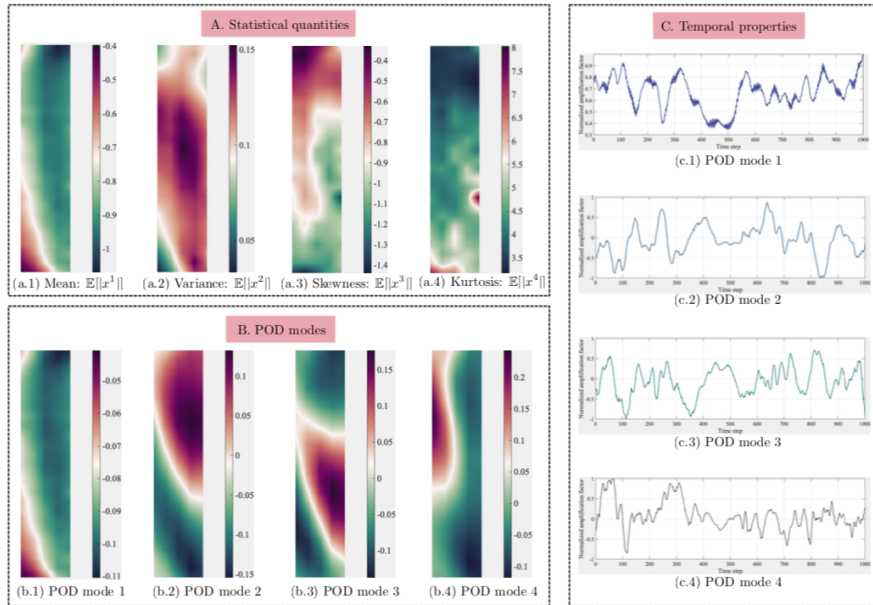


Figure 13: Leeward scenario: the decomposed spatial and temporal tensor by the POD algorithm.

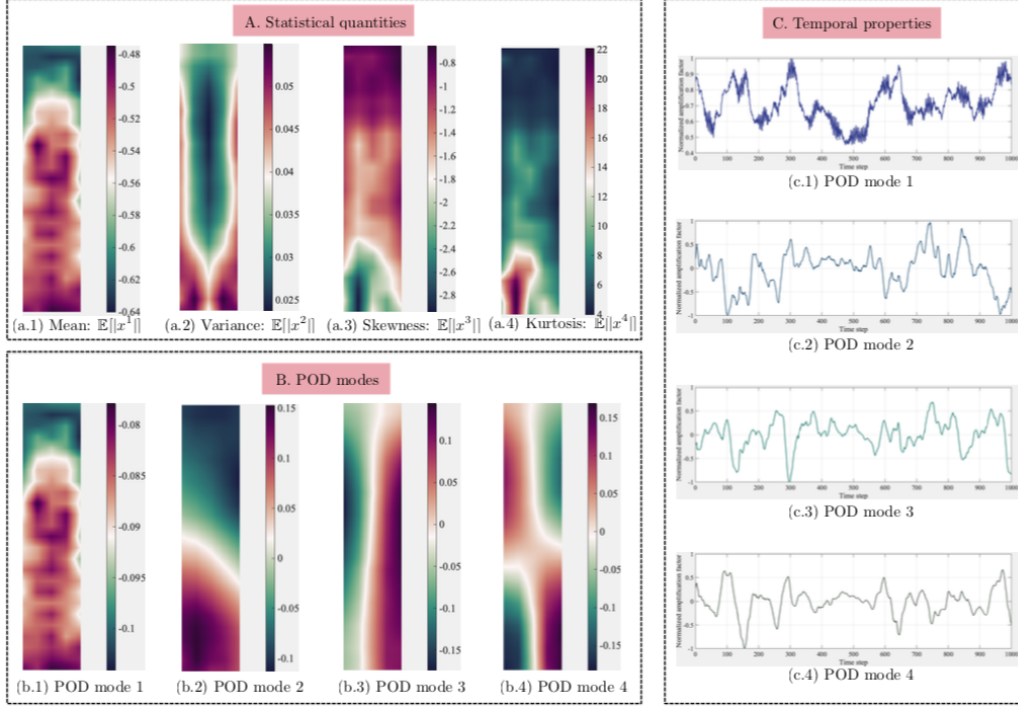


Figure 14: Rightside scenario: the decomposed spatial and temporal tensor by the POD algorithm.

4.4.2. DMD modes

Parameterization of DMD First and foremost, we define parameters involved in the augmented DMD algorithm utilizing the convergence and sufficiency analysis results presented earlier (See [Section 4.2.2](#) and [Section 4.3.2](#) for details). In particular, we use 730 snapshots to ensure obtaining converged results, leading to an input data matrix $\mathcal{D} \in \mathbb{R}^{125 \times 730}$. Then, we embed this matrix to a higher dimension by means of Takens's theorem [29, 31], where the embedding number $d = 30$. Such parameterization guarantees that most eigenvalues are driven to a neutrally stable state. The new input data matrix $\mathcal{D} \in \mathbb{R}^{3750 \times 701}$. According to [Eq. \(17\)](#) and [Eq. \(23\)](#), the augmented DMD algorithm divides \mathcal{D} into two time-shifted matrices $\mathbf{Y}, \mathbf{Y}' \in \mathbb{R}^{3750 \times 700}$. To conduct efficient decomposition analysis, we set the truncation number in the DMD method $r = 125$. Consequently, a low-rank representation consisting of 125 DMD modes is extracted by the proposed algorithm [21, 22]. To determine dynamically relevant DMD modes, we propose an unsupervised machine learning method, i.e., clustering to group DMD modes having sim-

ilar properties. In this context, the k-means clustering scheme, which is also known as Lloyd's method, is used as the algorithm can control the number of clusters [9, 44]. Inputs for the cluster analysis include the resolved 125 DMD eigenmodes and the cluster number $N_{cluster} = 3$. We normalize the eigenmode matrix to improve the clustering performance and the distance metric involved in the iterative calculation process is specified to the correlation type.

Inverse inference scheme After preprocessing, k-means clustering grouped the truncated 125 DMD eigenmodes into three clusters. It is found that each cluster is directly linked to a type of coherent structures categorized by the scale of spatial patterns, i.e. macro-scale, meso-scale, and micro-scale. From these three types of grouped coherent structures, we are interested in inferring the physical connections between clustered DMD modes and turbulent dynamics buried in the incoming winds. For example, it is known that the aerodynamic fluctuating wind loads acting on the windward face of the prism model is dominated by the atmospheric turbulence and wind loads acting on the two side and leeward faces are closely related to the wake excitations such as vortex shedding, which in turn are deeply influenced by the turbulent dynamics [6, 10, 11, 39]. These experimental findings show the feasibility of connecting the turbulence properties to the dynamic wind loads on structures represented by the combining use of the DMD modes and the temporal evolutions. However, it should be noted that such pattern-to-fluids inferring by definition is an inverse problem, imposing great challenges on distilling the hidden physical mechanisms [32, 34, 43]. To understand how turbulence affects a tall building, we focus on explaining the energy transfer (e.g. kinetic energy is dissipated into heat) within fluids by investigating the dynamical evolution of each DMD mode. In particular, the dynamical evolution of the identified coherent structures is compared with the energy transferring mechanisms of the atmospheric turbulence, which includes energy cascade, neutrally steady, and inverse cascade [37]. Furthermore, we attempt to connect identified spatial patterns to the length scales (eddy sizes) of the incoming turbulent flow since turbulence is an extremely complex process with a multitude of eddy scales and flow patterns [35]. Fig. 15 graphically highlights this inverse inference scheme.

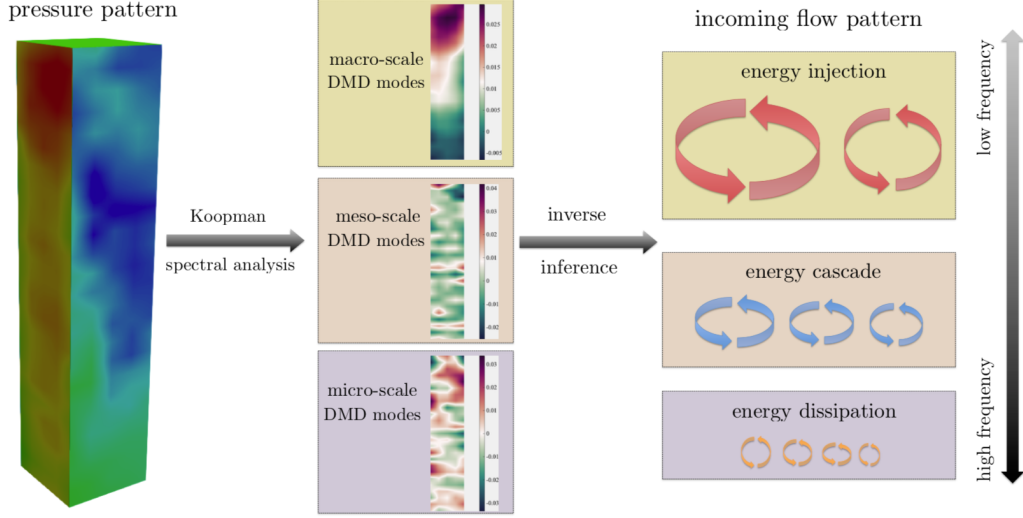


Figure 15: Inverse inference of clustered DMD modes.

Clustering results First, we have ranked the identified DMD modes by the real part of the eigenvalue in a descending order besides k-means clustering. We have classified 125 into three groups where group 1 is $\{\phi_1, \dots, \phi_{42}\}$, group 2 is $\{\phi_{43}, \dots, \phi_{84}\}$, and group 3 is $\{\phi_{85}, \dots, \phi_{125}\}$. Next, we compared the eigendecomposition results classified by the cluster analysis and physical ranking. Note every DMD mode has a unique eigenvalue that is complex valued, where the real part contains the information on the growth/decay rate and the imaginary part conveys the phase information. In Fig. 16, we first take the real part out and create a vector for each cluster, that is, $\Lambda^{macro} = [Re(\lambda_1), \dots, Re(\lambda_{n_{macro}})]$, $\Lambda^{meso} = [Re(\lambda_1), \dots, Re(\lambda_{n_{meso}})]$, and $\Lambda^{micro} = [Re(\lambda_1), \dots, Re(\lambda_{n_{micro}})]$. Then, distributions of Λ^{macro} , Λ^{meso} , and Λ^{micro} are approximated utilizing a normal kernel smoothing function. The same procedures have been applied to the ranking based group data. For a clear comparison purpose, we normalized the results by performing element-wise division where the divisor is $\max(Re(\lambda_i))$ with $i = 1, \dots, 125$. The upper row of Fig. 16 summarizes distribution results for different building surfaces. Obviously, macro-scale DMD modes tend to have larger eigenvalues, indicating that they contain more energy [3, 33], while eigenvalues of the micro-scale DMD modes spread over the entire interval. Secondly, each DMD mode is found oscillating at a specific frequency, which can be determined from the imaginary part of its eigenvalue. The second row of Fig. 16 gives distribution results of these frequencies of oscillation, where macro-

scale DMD modes have a relatively lower frequency range compared to the other two types. This observation agrees with the experimental finding on the turbulence of different length scales, where frequencies of large eddies are much smaller than small eddies [34, 37]. Moreover, the proposed supervised learning, clustering, have successfully grouped identified DMD modes by the similarity between two spatial patterns. The clustered results are in accordance with the physical ranking based on the magnitude of the real part of the eigenvalue.

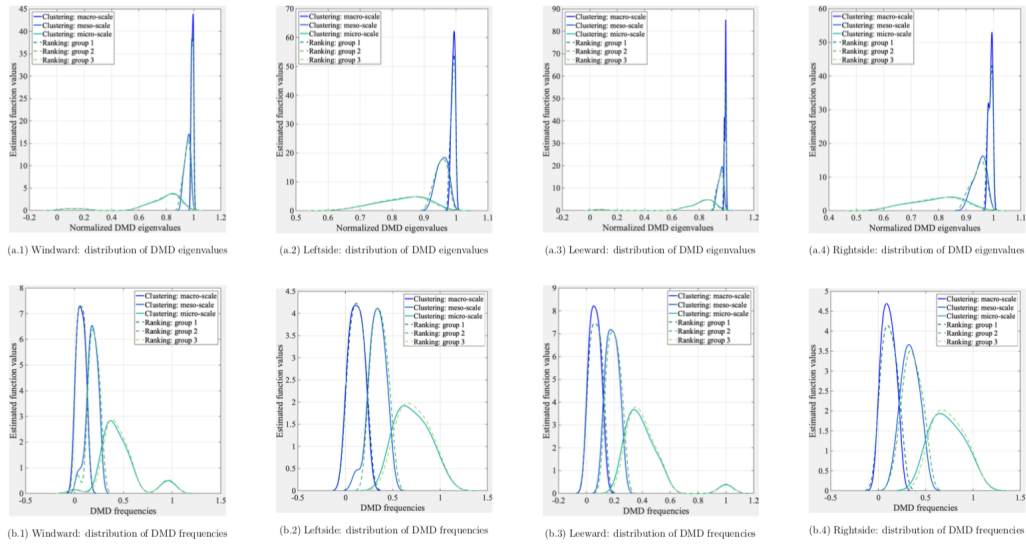


Figure 16: Distributions of clustered eigenvalues and frequencies.

Macro-scale DMD modes: connection with POD modes Similar to the POD modes ranked in descending order of energy content, we arrange the DMD modes based on their contributions to the total energy by means of the real parts $\text{Re}(\lambda_i)$. Fig. 17 summarizes the first four DMD modes of each surface. Even though there are differences between the POD and DMD modes, the identified eigenmodes share many similarities. In particular, the first DMD mode is notably related to the first POD mode. A general view of the resulting DMD modes shows that coherent structures at macro-scale provide a global sketch of the dynamic wind loads. Specifically, DMD modes in the windward scenario are in good agreement with the force pattern reasoning the overturning moment. The locations of local minima and maxima serve as scaled features of horizontal forces. The distinct separation of minimum and

maximum values indicate the moment on the windward surface computed using these horizontal forces directly contribute to the overall overturning moment. Moreover, the most energetic DMD modes in two side scenarios show the symmetry of the influence of macro-scale coherent structures is violated. The asymmetry factor causes the center of geometry and loading do not coincide, which in turn gives rise to the torsional loads. For the leeward, DMD mode 1 is obviously related to the overturning moment while the other three modes cover both overturning and torsional effects. Very similar results are also found in the POD modes [3, 6].

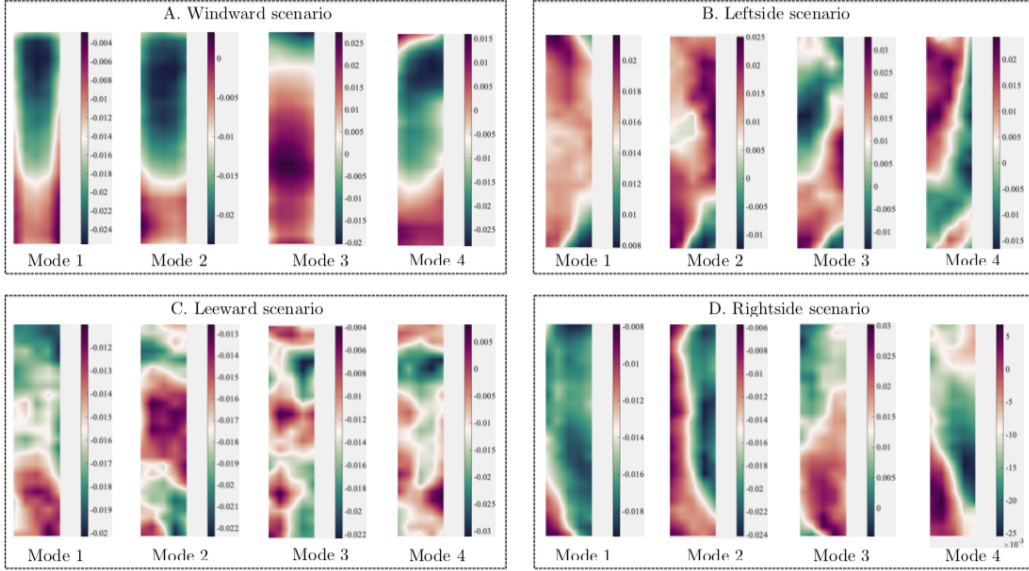


Figure 17: Macro-scale DMD modes.

Temporal evolution of macro-scale DMD modes: connection with mean flow field The most energetic modes obtained via the spectral analysis are usually connected with, to some extent, a collection of flow mechanisms such as the mean flow field around the object [45]. However, it should be noted that a particular Dmd mode may be simultaneously related to a few flow mechanisms. According to the results, we are mainly concerned with the mean flow field when analyzing the macro-scale DMD modes. First, it can be seen from Fig. 18 that the first DMD mode appears to grow in all scenarios. This observation conforms to the physical principles of the energy injection concerning stationary boundary layer winds [46],

where the continually incoming wind constitutes the mean energy injection that balances the mean energy dissipation. Secondly, other DMD modes mostly exhibit decay behavior in time. This is a strong resemblance to the turbulent energy cascade, where turbulent eddies of a wide range of scales passes energy consecutively from eddies of larger sizes to the smaller ones [47]. In the context of random pressure fields over tall buildings, macro-scale spatial patterns in DMD modes correspond to the large-scale fluid motions involved in the incoming wind. Observing at time t , the energy associated with these fluid motions is gradually dissipated by the kinematic viscosity according to the physical law [35], resulting in a decaying temporal behavior at $t + \Delta$, i.e. coherent structures at macro-scale decompose to a smaller scale (meso or micro). Hence, analyzing the temporal evolution of macro-scale DMD modes reveals the time-evolution of fluid flows caused by large eddies, which break down into turbulence.

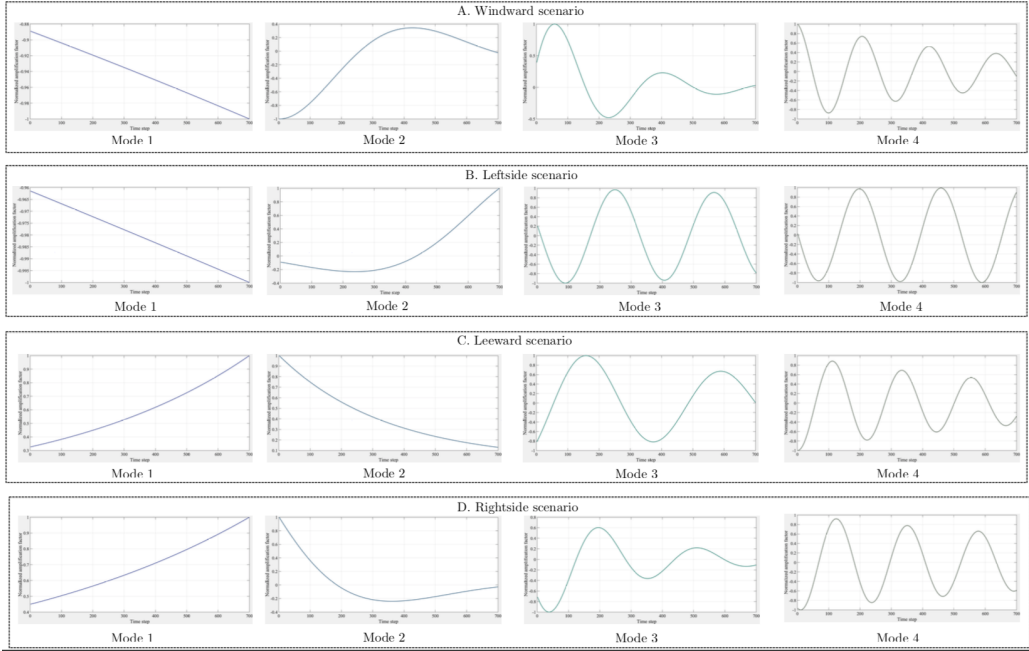


Figure 18: Dynamical evolution of selected macro-scale DMD modes.

Micro-scale DMD modes: connection with small eddies The dynamic wind forces are usually separated into mean and fluctuating components using the gust-factor approach [48]. And the fluctuating component related to the magnitude of pressure perturbations is directly affected by the

nearby small eddies. According to the Kolmogorov length scale theory, small eddies tend to have high frequencies, causing turbulence to be isotropic and homogeneous at a local scale [35]. In a generic sense, small eddies represent instabilities of local interactions between different fluid motions. In Fig. 19, we selected four micro-scale DMD modes from each scenario to illustrate such pressure perturbation. Two properties of the resulting DMD modes should be noted. First, pressure perturbations are randomly distributed on each surface. Secondly, the active areas are relatively small and sparsely scattered. These two properties conform to the characteristics of small eddies (randomness and size) [34, 35].

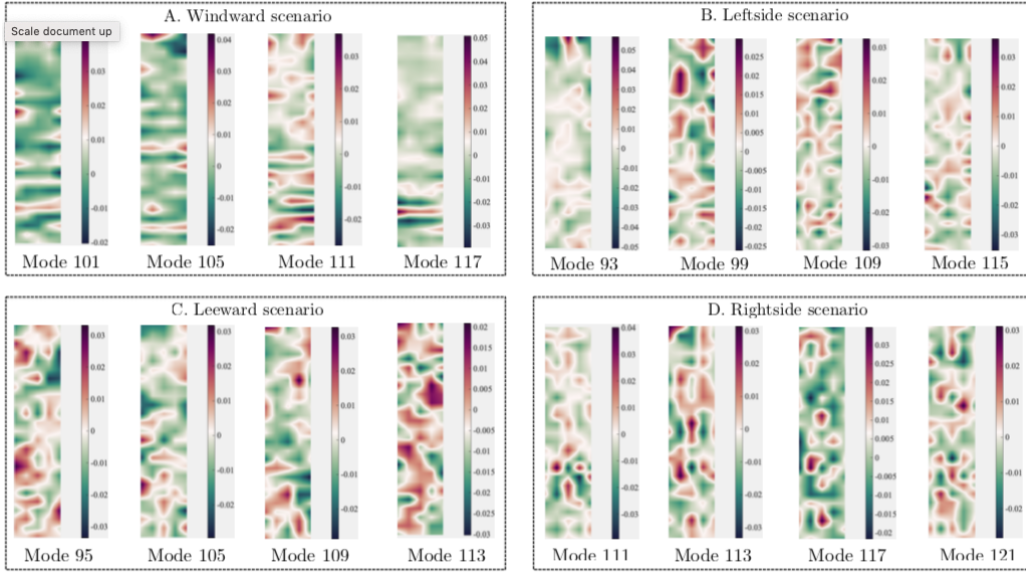


Figure 19: Micro-scale DMD modes.

Temporal evolution of micro-scale DMD modes: connection with energy dissipation From a physical standpoint, micro-scale DMD modes do not necessarily represent any specific flow patterns regarding the surrounding flow motions. In [45], it was pointed that the least energetic modes may contain information on the interaction between different mechanisms instead of actually representing one of them. Note this conclusion was drawn based on the POD method, which does not account for the temporal information. In Fig. 20, we summarize the temporal evolution of the selected micro-scale DMD modes. It can be clearly seen that all the selected

micro-scale DMD modes exhibit decay form. In particular, the amplitude of some modes decays exponentially, for instance, mode 111 of the windward and rightside face. This supports the turbulent energy cascade process where large eddies generated by the mean flow cascades down to small eddies, and the kinetic energy carried by small eddies ultimately dissipated to heat by viscous forces [46, 47].

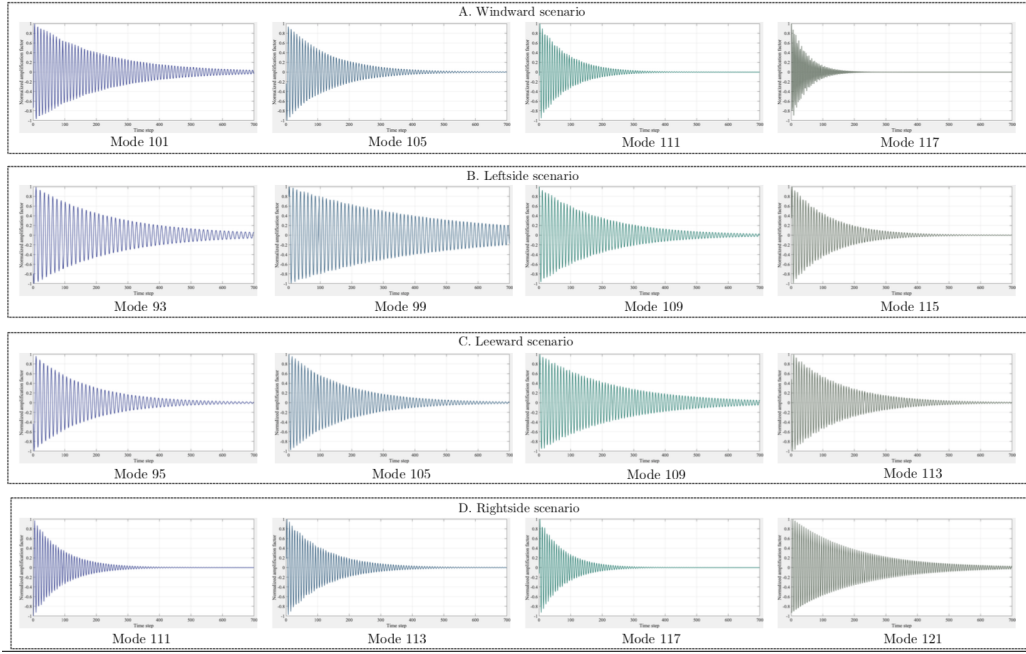


Figure 20: Dynamical evolution of selected micro-scale DMD modes.

Stripe pattern: connection with instantaneous pressure increment Wind loads acting on tall buildings are described by a random field that evolves in time, which means there is a pressure increment between instantaneous spatial pressure distribution measured at time t and $t + \Delta t$. An intuitive explanation of the pressure increment is based on the incoming flow that is the source of wind loading [2]. As it is illustrated in Fig. 21, small eddies induced fluid motions, that is, wind loads represented by the micro-scale DMD modes approach the tall building at the time t . Then, the small eddy rotates cyclonically like a rigid body, dynamically interacting with the building. Measuring at $t + \Delta t$, the active interface between the building and the wind can be graphically represented by the sketching stripe patterns. Be-

cause these stripe patterns are directly caused by the rotational movements of small eddies, which are spatially distributed all around the building, we can thereby observe such pattern in every surface.

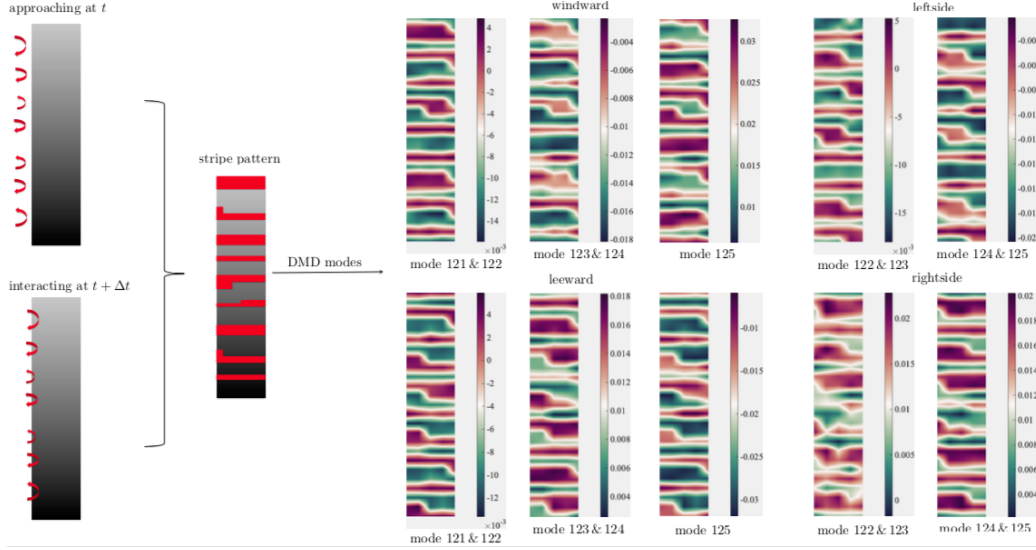


Figure 21: Illustration of the connection between micro-scale DMD modes and instantaneous increment of wind pressures.

Temporal evolution of the stripe pattern: connection with the beating phenomenon Eddies of different sizes have their corresponding points in a frequency spectrum of the turbulence. In Fig. 21, sizes of the stripe patterns are structurally similar, indicating the diameters of the surrounding eddies are very close. Consequently, the natural frequencies of these turbulent fluid motions interacting with the building are close. These factors naturally fulfill the precondition of the beating phenomenon, which in principle is a constructive interference pattern between two signals having almost identical frequencies [49]. The decomposition results describing the dynamical evolution of each stripe pattern mode are given in Fig. 22. The identified DMD modes oscillate up and down and the amplitudes are exhibiting a decaying pattern in a general sense. This is due to the fact that small eddies are gradually damped out by viscosity [35, 47]. Moreover, the beat phenomenon that is highlighted by the red dots only happens in the high-frequency region (See Fig. 23). An intuitive explanation is based on the definition of the beating phenomenon, which not only requires the existence

of two fluid motions sharing similar frequencies but also expects these two eddies are closely located in space. However, lower frequencies are associated with larger fluid motions that are energetically unstable [37]. This fundamental fact makes observing the beating phenomenon in the low-frequency region a statistically rare event.

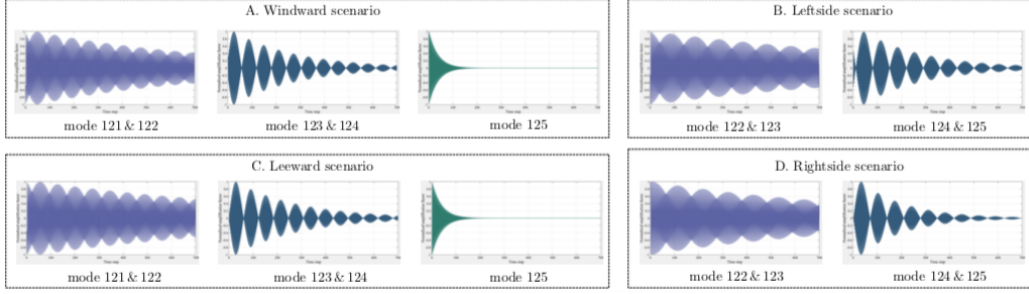


Figure 22: Dynamical evolution of selected micro-scale DMD modes.

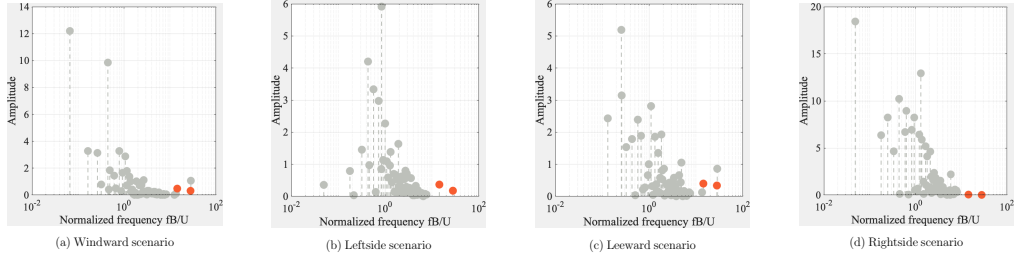


Figure 23: Spectra properties of DMD results. The red dots denote the beating phenomenon.

Connection with discrete fourier transform In [25], it is found that DMD provides identical results to the temporal discrete Fourier transform (DFT) if the input data is linearly independent and zero centered. Despite the fact that our wind pressure data is highly nonlinear and the mean subtraction is skipped, DMD spectrum can recover dynamics of the wind pressure data from the frequency aspect. We plot the mode amplitude as a function of frequency, which can be computed from the imaginary part of the DMD eigenvalues. Such spectrum captures the magnitude and phase of pressure dynamics through a linear combination of eigenvectors, where every eigenvector grows or decays at a specified frequency according to its associated

eigenvalue. For comparison, we further compute the amplitude of oscillations at a wide range of frequencies by means of the Fourier transform, where the temporal DFT model is essentially a superposition of a series of harmonic oscillators. Fig. 24 shows that the DMD spectrum closely resembles the FFT spectrum. The proposed augmented DMD algorithm accurately captures the leading amplitudes of the power spectrum computed by the FFT. Moreover, it should be noted that the FFT spectrum is computed independently using the collected time series data recorded via each pressure tap. On the contrary, every single point in the DMD spectrum denotes a certain coherent structure covering 125 pressure taps over a specific surface.

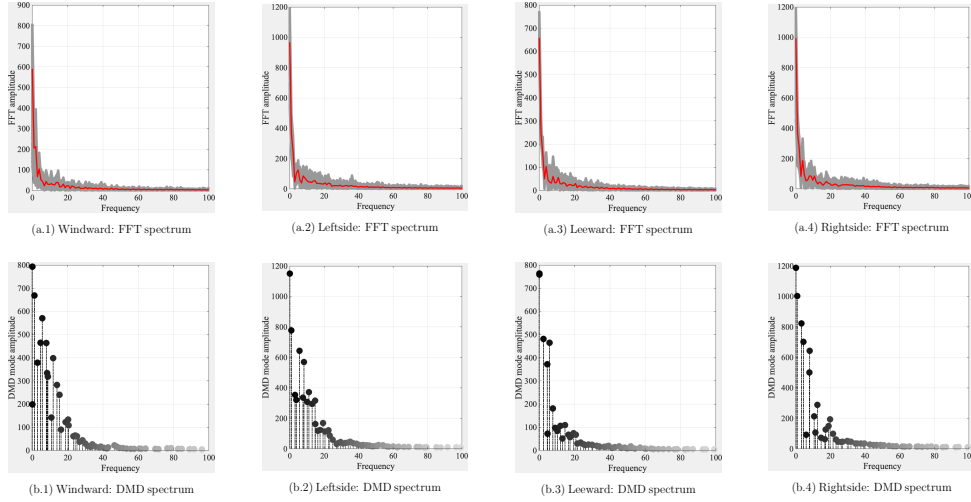


Figure 24: FFT and DMD spectrum. In the FFT spectrum representations, the gray band illustrates the discrete Fourier transform (DFT) results of 125 time-ordered sequences using a fast Fourier transform (FFT) algorithm and the red line denotes their mean.

5. Concluding remarks

In this paper, an operator-theoretic method is introduced to dynamical systems analysis, with emphasis on the transient mapping of the evolution process. Compared to the state-space method, the operator-theoretic modeling characterizes the evolution mechanism of a nonlinear/chaotic system via an infinite-dimensional linear operator, i.e. nonlinear dynamics is linearized in the entire basin without sacrificing computational accuracy. This is accomplished by the spectral analysis of the Koopman operator, which lifts a

dynamical system from phase space to Hilbert function space. In particular, the dynamic mode decomposition (DMD) is used to obtain the Koopman eigen-tuple. We have demonstrated our system identification scheme using random wind pressure fields over faces of a scaled model of a finite height prism representing a tall building, where the data is derived from wind tunnel tests. To improve the algorithm’s performance, Takens embedding theorem is incorporated into the learning scheme, reinforcing the capacity of dynamical mechanisms buried in data against noisy signals.

A comparative study between classical POD and proposed augmented DMD is carried out with application to a high-dimensional random pressure field, which is continually evolving in time through a differential operator. The POD is limited to producing a set of hierarchically structured eigenmodes in terms of the time-averaged spatial tensor, and each mode is randomly evolving in time. On the contrary, the DMD representation is orthogonal in both spatial and temporal directions where each identified coherent structure is assigned to a specific frequency and a corresponding growth/decay rate.

The proposed operator-theoretic method provides an in-depth understanding of the wind structure interactions governed by the evolution operator in addition to an accurate aerodynamic characterization of a wind event. Specifically, direct connections have been established between identified DMD modes and eddy structures in turbulence. Macro-scale coherent structures are found to be energetically unstable and prone to producing energy decay, similar to the turbulent cascade. And micro-scale coherent structures are closely connected to the instantaneous pressure increment as their associated frequencies are relatively higher. These results provide physical insights to the inverse modeling, i.e., from the description of dynamic pressures to the characterization of incoming turbulence in wind.

Future directions regarding applying the Koopman operator to learn non-linear dynamical systems include: (1) Extension of the current work to the extreme learning condition where available data is merely a sequence of a scalar, and (2) Moving from the current Laplacian determinism and learning the intrinsic orderliness governing a chaotic system.

6. Reference

References

- [1] M. Shinozuka, C.-M. Jan, Digital simulation of random processes and its applications, *Journal of sound and vibration* 25 (1) (1972) 111–128.
- [2] A. Kareem, Numerical simulation of wind effects: a probabilistic perspective, *Journal of Wind Engineering and Industrial Aerodynamics* 96 (10-11) (2008) 1472–1497.
- [3] A. Kareem, J. Cermak, Pressure fluctuations on a square building model in boundary-layer flows, *Journal of Wind Engineering and Industrial Aerodynamics* 16 (1) (1984) 17–41.
- [4] Y. Tamura, S. Suganuma, H. Kikuchi, K. Hibi, Proper orthogonal decomposition of random wind pressure field, *Journal of Fluids and Structures* 13 (7-8) (1999) 1069–1095.
- [5] X. Chen, A. Kareem, Proper orthogonal decomposition-based modeling, analysis, and simulation of dynamic wind load effects on structures, *Journal of Engineering Mechanics* 131 (4) (2005) 325–339.
- [6] B. Kim, K. Tse, Y. Tamura, Pod analysis for aerodynamic characteristics of tall linked buildings, *Journal of Wind Engineering and Industrial Aerodynamics* 181 (2018) 126–140.
- [7] G. Solari, L. Carassale, F. Tubino, Proper orthogonal decomposition in wind engineering. part 1: A state-of-the-art and some prospects, *Wind and Structures* 10 (2) (2007) 153–176.
- [8] I. Jolliffe, *Principal component analysis*, Springer, 2011.
- [9] K. P. Murphy, *Machine learning: a probabilistic perspective*, MIT press, 2012.
- [10] L. Carassale, M. M. Brunenghi, Statistical analysis of wind-induced pressure fields: A methodological perspective, *Journal of Wind Engineering and Industrial Aerodynamics* 99 (6-7) (2011) 700–710.
- [11] L. Carassale, Analysis of aerodynamic pressure measurements by dynamic coherent structures, *Probabilistic Engineering Mechanics* 28 (2012) 66–74.

- [12] L. Perko, Differential equations and dynamical systems, Vol. 7, Springer Science & Business Media, 2013.
- [13] J. N. Kutz, S. L. Brunton, B. W. Brunton, J. L. Proctor, Dynamic mode decomposition: data-driven modeling of complex systems, Vol. 149, Siam, 2016.
- [14] I. Mezić, Spectral properties of dynamical systems, model reduction and decompositions, *Nonlinear Dynamics* 41 (1-3) (2005) 309–325.
- [15] D. Giannakis, Data-driven spectral decomposition and forecasting of ergodic dynamical systems, *Applied and Computational Harmonic Analysis*.
- [16] S. Klus, F. Nüske, P. Koltai, H. Wu, I. Kevrekidis, C. Schütte, F. Noé, Data-driven model reduction and transfer operator approximation, *Journal of Nonlinear Science* 28 (3) (2018) 985–1010.
- [17] B. O. Koopman, Hamiltonian systems and transformation in hilbert space, *Proceedings of the National Academy of Sciences* 17 (5) (1931) 315–318.
- [18] M. Budišić, R. Mohr, I. Mezić, Applied koopmanism, *Chaos: An Interdisciplinary Journal of Nonlinear Science* 22 (4) (2012) 047510.
- [19] I. Mezić, Analysis of fluid flows via spectral properties of the koopman operator, *Annual Review of Fluid Mechanics* 45 (2013) 357–378.
- [20] R. M. Mohr, Spectral Properties of the Koopman Operator in the Analysis of Nonstationary Dynamical Systems, University of California, Santa Barbara, 2014.
- [21] P. J. Schmid, Dynamic mode decomposition of numerical and experimental data, *Journal of fluid mechanics* 656 (2010) 5–28.
- [22] C. W. Rowley, I. Mezić, S. Bagheri, P. Schlatter, D. S. Henningson, Spectral analysis of nonlinear flows, *Journal of fluid mechanics* 641 (2009) 115–127.
- [23] J. H. Tu, C. W. Rowley, D. M. Luchtenburg, S. L. Brunton, J. N. Kutz, On dynamic mode decomposition: theory and applications, arXiv preprint arXiv:1312.0041.

- [24] M. O. Williams, I. G. Kevrekidis, C. W. Rowley, A data-driven approximation of the koopman operator: Extending dynamic mode decomposition, *Journal of Nonlinear Science* 25 (6) (2015) 1307–1346.
- [25] K. K. Chen, J. H. Tu, C. W. Rowley, Variants of dynamic mode decomposition: boundary condition, koopman, and fourier analyses, *Journal of nonlinear science* 22 (6) (2012) 887–915.
- [26] T. W. Muld, G. Efraimsson, D. S. Henningson, Mode decomposition on surface-mounted cube, *Flow, turbulence and combustion* 88 (3) (2012) 279–310.
- [27] T. W. Muld, G. Efraimsson, D. S. Henningson, Flow structures around a high-speed train extracted using proper orthogonal decomposition and dynamic mode decomposition, *Computers & Fluids* 57 (2012) 87–97.
- [28] Tpu aerodynamic database: Wind pressure database based on wind tunnel experiment for high-rise building (<http://wind.arch.t-kougei.ac.jp/system/eng/contents/code/tpu>).
- [29] F. Takens, Detecting strange attractors in turbulence, in: *Dynamical systems and turbulence*, Warwick 1980, Springer, 1981, pp. 366–381.
- [30] N. Takeishi, Y. Kawahara, T. Yairi, Learning koopman invariant subspaces for dynamic mode decomposition, in: *Advances in Neural Information Processing Systems*, 2017, pp. 1130–1140.
- [31] S. Le Clainche, J. M. Vega, Higher order dynamic mode decomposition, *SIAM Journal on Applied Dynamical Systems* 16 (2) (2017) 882–925.
- [32] X. Chen, A. Kareem, Equivalent static wind loads on buildings: New model, *Journal of Structural Engineering* 130 (10) (2004) 1425–1435.
- [33] N. Lin, C. Letchford, Y. Tamura, B. Liang, O. Nakamura, Characteristics of wind forces acting on tall buildings, *Journal of Wind Engineering and Industrial Aerodynamics* 93 (3) (2005) 217–242.
- [34] H. Tennekes, J. L. Lumley, J. Lumley, et al., *A first course in turbulence*, MIT press, 1972.
- [35] U. Frisch, A. Kolmogorov, *Turbulence: the legacy of AN Kolmogorov*.

- [36] L. Wang, M. McCullough, A. Kareem, A data-driven approach for simulation of full-scale downburst wind speeds, *Journal of Wind Engineering and Industrial Aerodynamics* 123 (2013) 171–190.
- [37] A. J. Majda, Y. Lee, Conceptual dynamical models for turbulence, *Proceedings of the National Academy of Sciences* 111 (18) (2014) 6548–6553.
- [38] T. Stathopoulos, Wind loads on low-rise buildings: a review of the state of the art, *Engineering Structures* 6 (2) (1984) 119–135.
- [39] T. Tamura, Y. Ono, Les analysis on aeroelastic instability of prisms in turbulent flow, *Journal of wind engineering and industrial aerodynamics* 91 (12-15) (2003) 1827–1846.
- [40] C. W. Rowley, T. Colonius, R. M. Murray, Model reduction for compressible flows using pod and galerkin projection, *Physica D: Nonlinear Phenomena* 189 (1-2) (2004) 115–129.
- [41] K. Carlberg, C. Bou-Mosleh, C. Farhat, Efficient non-linear model reduction via a least-squares petrov–galerkin projection and compressive tensor approximations, *International Journal for Numerical Methods in Engineering* 86 (2) (2011) 155–181.
- [42] B. Lusch, J. N. Kutz, S. L. Brunton, Deep learning for universal linear embeddings of nonlinear dynamics, *Nature communications* 9 (1) (2018) 4950.
- [43] J. H. Ferziger, M. Peric, *Computational methods for fluid dynamics*, Springer Science & Business Media, 2012.
- [44] D. Arthur, S. Vassilvitskii, k-means++: The advantages of careful seeding, in: *Proceedings of the eighteenth annual ACM-SIAM symposium on Discrete algorithms*, Society for Industrial and Applied Mathematics, 2007, pp. 1027–1035.
- [45] C. Baker, Aspects of the use of proper orthogonal decomposition of surface pressure fields, *Wind and Structures* 3 (2) (2000) 97–115.
- [46] O. Cadot, Y. Couder, A. Daerr, S. Douady, A. Tsinober, Energy injection in closed turbulent flows: Stirring through boundary layers versus inertial stirring, *Physical Review E* 56 (1) (1997) 427.

- [47] A. Leonard, Energy cascade in large-eddy simulations of turbulent fluid flows, in: Advances in geophysics, Vol. 18, Elsevier, 1975, pp. 237–248.
- [48] A. Kareem, Y. Zhou, Gust loading factorpast, present and future, Journal of Wind Engineering and Industrial Aerodynamics 91 (12-15) (2003) 1301–1328.
- [49] S. K. Yalla, A. Kareem, Beat phenomenon in combined structure-liquid damper systems, Engineering Structures 23 (6) (2001) 622–630.

A. Appendix

This appendix provides a quick summary of the proper orthogonal decomposition (POD) method that analyzes chaotic data from a conventional variance optimization perspective. Then, the POD results are compared with those obtained via the proposed augmented dynamic mode decomposition method, illustrating the unique characteristics of each method (See [Section 4](#) for a detailed comparison study).

To begin with, let \mathbf{C}_p denote the spatial-temporal pressure coefficient data obtained from a synchronous measurement system in wind tunnel. Under finite energy assumption $\int_{\Omega_T} \int_{\Omega_x} |\mathbf{C}_p|^2 d\mathbf{x}dt < \infty$, $\mathbf{C}_p(\mathbf{x}, t)$ belongs to the Hilbert space $\mathcal{H} = L^2(\Omega_T \times \Omega_x)$ of Lebesgue measurable. Because the tensor space is dense in $L^2(\Omega_T \times \Omega_x)$, \mathbf{C}_p takes a tensor product form:

$$\mathbf{C}_p(\mathbf{x}, t) = \mathcal{A}(\Omega_T) \otimes \Phi(\Omega_x) \quad (\text{A.1})$$

where $\mathcal{A}(\Omega_T) \doteq L^2(\Omega_T)$, $\Phi(\Omega_x) \doteq L^2(\Omega_x)$, Ω_x represents the spatial domain. As a result, the spatiotemporal representation of $\mathbf{C}_p(\mathbf{x}, t)$ is explicitly converted to a bilinear composition form, with the first vector space \mathcal{A} producing the time-dependent coefficients and the second vector space Φ giving spatial modes. Mathematically speaking, the preceding equation can be equivalently expressed as a linear superposition using a complete set of basis functions according to the Schmidt decomposition theorem:

$$\mathbf{C}_p(\mathbf{x}, t) = \sum_{j=1}^N a_j(t) \phi_j(x) \quad (\text{A.2})$$

Unfortunately, N is a considerably large number or infinity in most cases. The essence of POD is to seek an orthogonal projector $\mathbf{v}(\mathbf{x}, t)$ that minimizes the approximation error:

$$\mathcal{J}(\mathbf{v}) = \|\mathbf{C}_p(\mathbf{x}, t) - \mathbf{v}(\mathbf{x}, t)\|_{n_F} \quad (\text{A.3})$$

with $\|\cdot\|_{n_F}$ denoting the Frobenius norm. In the context of POD, $n_F = 2$, which guarantees the kinetic energy interpretation of its optimized modes $\phi_j, j = 1, 2, \dots, N$, and the projector $\mathbf{v}(\mathbf{x}, t)$ can be directly constructed through utilizing a finite set of orthogonal basis functions ($M \ll N$) following the principles stated in Eq. (A.2):

$$\mathbf{C}_p(\mathbf{x}, t) \approx \mathbf{v}(\mathbf{x}, t) = \sum_{j=1}^M a_j(t) \phi_j(\mathbf{x}) \quad (\text{A.4})$$

Then, the optimal basis functions can be obtained by maximizing the average projection of $\mathbf{C}_p(\mathbf{x}, t)$ onto Φ :

$$\arg \max \frac{\langle \mathbf{C}_p, \Phi(\mathbf{x}) \rangle_{\Omega_x}}{\langle \Phi(\mathbf{x}), \Phi(\mathbf{x}) \rangle_{\Omega_x}} \quad (\text{A.5})$$

By applying the calculus of variations, the optimization problem stated in Eq. (A.5) is transformed to a Fredholm eigenvalue setting, where the optimal POD basis is exactly the eigenfunctions in the following integral equation:

$$\int_{\Omega_x} R(\mathbf{x}, \mathbf{x}') \phi_j(\mathbf{x}') d\mathbf{x}' = \lambda_j \phi_j(\mathbf{x}) \quad (\text{A.6})$$

where $R(\mathbf{x}, \mathbf{x}')$ is the symmetric spatial correlation tensor that is computed by taking the inner product of the pressure data in Ω_x :

$$R(\mathbf{x}, \mathbf{x}') = \langle \mathbf{v}(\mathbf{x}, t) \otimes \mathbf{v}(\mathbf{x}', t) \rangle_{\Omega_x} \quad (\text{A.7})$$

Two important properties associated with Eq. (A.6) should be observed. First, Hilbert-Schmidt theory assures the eigenvalue problem has an infinitely countable pair of eigenfunctions and eigenvalues $\{\phi_j, \lambda_j\}$, out of which there exists a sequence of positive eigenvalues $\lambda_1 \geq \lambda_2 \geq \dots \geq 0$. POD modes are ranked according to the eigenvalues of $R(\mathbf{x}, \mathbf{x}') \phi_j(\mathbf{x}')$ by a descending order. Second, eigenfunctions are orthogonal $\int_{\Omega_x} \phi_i(\mathbf{x}) \phi_j(\mathbf{x}) d\mathbf{x} = \delta_{ij}$, implying the POD algorithm seeks the least number of modes for capturing $\mathbf{C}_p(\mathbf{x}, t)$.